The Astrophysical Journal, 961:169 (24pp), 2024 February 1 https://doi.org/10.3847/1538-4357/ad12be

An Extensive Hubble Space Telescope Study of the Offset and Host Light Distributions of Type I Superluminous Supernovae

Brian Hsu[1,2], Peter K. Blanchard[3], Edo Berger[1,4], and Sebastian Gomez[5]
[1] Center for Astrophysics Harvard & Smithsonian, 60 Garden Street, Cambridge, MA 02138-1516, USA; bhsu@arizona.edu
[2] Steward Observatory, University of Arizona, 933 North Cherry Avenue, Tucson, AZ 85721-0065, USA
[3] Center for Interdisciplinary Exploration and Research in Astrophysics and Department of Physics and Astronomy, Northwestern University, 1800 Sherman Avenue, 8th Floor, Evanston, IL 60201, USA
[4] The NSF AI Institute for Artificial Intelligence and Fundamental Interactions, Cambridge, MA 02139, USA
[5] Space Telescope Science Institute, 3700 San Martin Drive, Baltimore, MD 21218, USA
Received 2023 August 14; revised 2023 December 1; accepted 2023 December 3; published 2024 January 24

Abstract

We present an extensive Hubble Space Telescope rest-frame UV imaging study of the locations of Type I superluminous supernovae (SLSNe) within their host galaxies. The sample includes 65 SLSNe with detected host galaxies in the redshift range $z \approx 0.05$–2. Using precise astrometric matching with SN images, we determine the distributions of the physical and host-normalized offsets relative to the host centers, as well as the fractional flux distribution relative to the underlying UV light distributions. We find that the host-normalized offsets of SLSNe roughly track an exponential disk profile, but exhibit an overabundance of sources with large offsets of 1.5–4 times their hosts' half-light radii. The SLSNe normalized offsets are systematically larger than those of long gamma-ray bursts (LGRBs), and even Type Ib/c and Type II SNe. Furthermore, we find from a Monte Carlo procedure that about 37^{+6}_{-8}% of SLSNe occur in the dimmest regions of their host galaxies, with a median fractional flux value of 0.16, in stark contrast to LGRBs and Type Ib/c and Type II SNe. We do not detect any significant trends in the locations of SLSNe as a function of redshift, or as a function of explosion and magnetar engine parameters inferred from modeling of their optical light curves. The significant difference in SLSN locations compared to LGRBs (and normal core-collapse SNe) suggests that at least some of their progenitors follow a different evolutionary path. We speculate that SLSNe arise from massive runaway stars from disrupted binary systems, with velocities of $\sim 10^2$ km s^{-1}.

Unified Astronomy Thesaurus concepts: Stellar populations (1622); Supernovae (1668)

1. Introduction

Hydrogen-poor (Type I) superluminous supernovae (SLSNe; Chomiuk et al. 2011; Quimby et al. 2011; Gal-Yam 2012) are a rare subclass of core-collapse supernovae (CCSNe) that are ∼10–100 times more luminous than normal SNe and have longer durations of several months to years (e.g., Nicholl et al. 2015; Inserra et al. 2017; De Cia et al. 2018; Lunnan et al. 2018). Originally defined to have a peak absolute magnitude of $M < -21$ (Gal-Yam 2012), they are now classified based on their spectra, which are dominated by a blue continuum devoid of hydrogen features, and typically exhibit distinctive early-time, "W-shaped" O II absorption lines at ∼3600–4600 Å (Chomiuk et al. 2011; Quimby et al. 2011; Lunnan et al. 2013; Mazzali et al. 2016; Quimby et al. 2018). The volumetric rate of SLSNe is only ∼0.1% of the overall CCSN rate (Quimby et al. 2018; Frohmaier et al. 2021), but in magnitude-limited optical surveys they account for ∼2% of all transients (e.g., Villar et al. 2019; Perley et al. 2020; Gomez et al. 2021) thanks to their high luminosities.

Shortly after their discovery, it became clear that SLSNe are not powered by the radioactive decay of ^{56}Ni (Arnett 1982) as in Type Ib/c SNe (SNe Ib/c). This is due to the unusually high fraction of radioactive nickel required to match the observed luminosity and timescales, with the total nickel mass often exceeding the total ejecta mass, in conflict with the lack of suppression of their UV emission due to line blanketing from iron-peak elements (e.g., Dessart et al. 2012; Inserra et al. 2013; Nicholl et al. 2013, 2017a, 2017c; Yan et al. 2017b; Liu et al. 2017; Gal-Yam 2019). Instead, alternative mechanisms have been proposed as the main power source of SLSNe, including a central engine with a rapidly spinning (∼few milliseconds) and highly magnetized (∼10^{14} G) neutron star (i.e., the magnetar model; Kasen & Bildsten 2010; Woosley 2010; Dessart et al. 2012; Metzger et al. 2015; Nicholl et al. 2017c), or shock interaction with a hydrogen-poor circumstellar medium (i.e., the CSM model; Chevalier & Irwin 2011; Chatzopoulos et al. 2012).

The magnetar model has been highly successful in accounting for the broad range of peak luminosities and timescales (e.g., Nicholl et al. 2017c; Blanchard et al. 2020; Hsu et al. 2021), for early UV/optical spectra (e.g., Nicholl et al. 2017b), for nebular-phase spectra (e.g., Nicholl et al. 2016, 2019; Jerkstrand et al. 2017), and for the power-law decline rates observed in SN 2015bn and SN 2016inl at $\gtrsim 10^3$ days (Nicholl et al. 2018; Blanchard et al. 2021). On the other hand, there are a handful of events supporting CSM interaction as the dominant power source for SLSNe based on the presence of interaction lines (e.g., Yan et al. 2015, 2017a) and equally well-explained light curves (e.g., Chatzopoulos et al. 2012; Chen et al. 2022b). However, the spectroscopic properties exhibited by the majority of SLSNe (e.g., Pastorello et al. 2010; Quimby et al. 2011, 2018; Inserra et al. 2013; Liu et al. 2017) and limits placed by X-ray/radio observations (Margutti et al.

2018; Eftekhari et al. 2021) are hard to reconcile with the CSM model alone.

In addition to the power source of SLSNe, it is critical to explore and constrain possible progenitor systems. The lack of hydrogen spectral features in SLSNe point to a connection with the stripped-envelope massive-star progenitors of SNe Ib/c (e.g., Pastorello et al. 2010). However, it has been shown with a uniformly modeled light curve sample that SLSN progenitors are systematically more massive (≈3.6–40 $M_\odot$; Blanchard et al. 2020) than SNe Ib/c progenitors (≈3.7–5.4 $M_\odot$; Barbarino et al. 2020). Comparing the SLSN progenitor mass distribution at the time of explosion to stellar evolutionary models suggests that low-metallicity binary systems may be plausible progenitors (e.g., Liu et al. 2015; Moriya et al. 2015; Blanchard et al. 2020; Stevance & Eldridge 2021).

Studies of SLSN host galaxies have also been leveraged to shed light on their progenitors. These studies revealed a preference for low-metallicity dwarf galaxies with higher specific star formation rates (sSFRs) and lower luminosities than CCSNe (e.g., Chen et al. 2013; Lunnan et al. 2013, 2014, 2015; Angus et al. 2016; Perley et al. 2016; Schulze et al. 2018). An investigation of the subgalactic environments of 16 SLSNe using high-resolution Hubble Space Telescope (HST) data suggested that SLSN locations track bright UV regions of their host galaxies (Lunnan et al. 2015; hereafter L15), consistent with massive progenitors. The relatively small sample size, however, did not allow for a statistically meaningful comparison with other classes of transients such as long gamma-ray bursts (LGRBs) and CCSNe.

With about 150 spectroscopically confirmed SLSNe to date (Gomez et al. 2020; Chen et al. 2022a), it is now possible to expand significantly on the early analysis of SLSN locations (L15). Here, we take advantage of a large set of archival HST SLSN host galaxy rest-frame UV observations from a wide range of programs, to produce the first large (65 SLSNe) and statistically meaningful sample of SLSN subgalactic locations. We follow the same methodology that has been employed to explore the progenitors of other populations of transients, including Type Ia SNe (Wang et al. 2013; Anderson et al. 2015), SNe Ib/c and Type II SNe (SNe II; Kelly et al. 2008; Prieto et al. 2008; Svensson et al. 2010; Kelly & Kirshner 2012), LGRBs (Bloom et al. 2002; Fruchter et al. 2006; Svensson et al. 2010; Blanchard et al. 2016, hereafter B16), and short GRBs (Fong & Berger 2013).

The paper is structured as follows. We present the sample, HST imaging, data processing techniques, and astrometric matching to determine the SLSN locations in Section 2. In Section 3 we describe our measurement methodology for determining host associations, offsets, and fractional fluxes. In Section 4 we present the resulting offset and fractional flux distributions and compare these to other transients. In Section 5 we explore trends and correlations with redshift, as well as with inferred SLSN explosion and magnetar engine properties, and discuss implications for SLSN progenitors. We conclude with a summary of our findings in Section 6.

Throughout the paper, we assume a flat Lambda cold dark matter (ΛCDM) cosmology with $\Omega_m = 0.310$ and $H_0 = 67.7\,\mathrm{km\,s^{-1}}$ Mpc, based on the Planck 2018 results (Planck Collaboration et al. 2020). All observations are reported in AB magnitudes (Oke & Gunn 1983) and corrected for Galactic extinction using Schlafly & Finkbeiner (2011), following the Gordon et al. (2023) extinction law with $R_V = 3.1$.

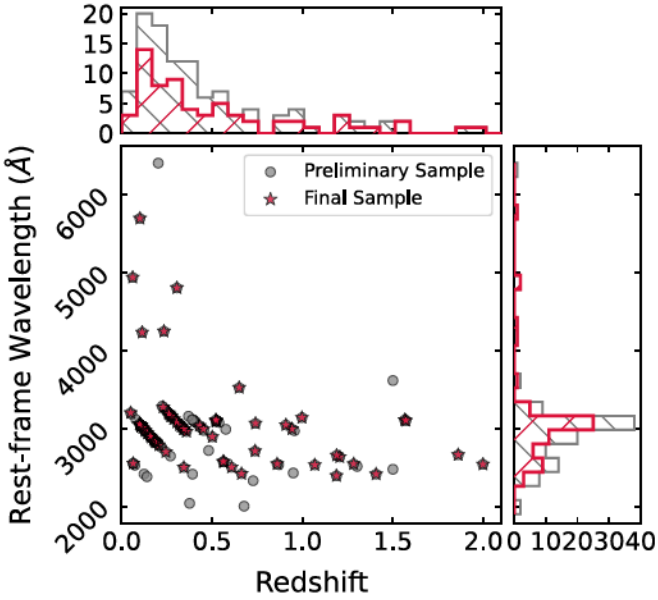

Figure 1. Rest-frame effective wavelengths probed by the HST data as a function of SLSN redshift. Gray points denote the full sample, while red points indicate the final sample used in the analysis (see Section 2). We note that only 5/65 SLSN hosts in the final sample are not observed at rest-frame UV. The top and right panels show the projected distributions of redshift and rest-frame wavelength, respectively.

2. Data and Astrometry

2.1. HST Data

We compiled an initial sample of 109 Type I SLSNe with HST host galaxy observations from archival and ongoing programs, imaged with either the Advanced Camera for Surveys (ACS) or the Wide Field Camera 3 (WFC3). The names, redshifts, and details of the HST observations are listed in Table 1. The initial sample spans a wide redshift range of $z = (0.05–1.998)$, where the HST filters used in the observations predominantly probe a rest-frame wavelength range in the UV of ≈2300–3300 Å; see Figure 1. This allows us to probe the locations of the SLSNe relative to the underlying star formation activity in their hosts.

We obtained the HST data from the Mikulski Archive for Space Telescopes (MAST[6]), and retrieved charge transfer efficiency (CTE) corrected images with `astroquery`. The majority of observations were obtained with a standard four-point dither pattern for optimal pixel subsampling during a single visit, while some have either a two-point pattern, a three-point pattern, or multiple visits in the same filter. By combining dithered exposures, we reconstruct a final image for each host galaxy with higher resolution than the original ones sampled by the instrumental point-spread function (PSF). We further apply distortion corrections, which improve the precision of our astrometric alignment. The CTE-corrected images were processed and combined with the `AstroDrizzle` task as a part of the `DrizzlePac` software package provided by STScI (Gonzaga et al. 2012). We use `final_pixfrac` = 0.8 or 0.9 depending on the pixel variation of the output image, and `final_scale` = 0.″020 and 0.″025 pixel^{-1}[7] for WFC3/UVIS and ACS, respectively. All the HST data used in this paper can be found in MAST at doi:10.17909/skn3-8756.

[6] https://archive.stsci.edu

[7] Except for PS1-11aib, for which we keep the original pixel scale of 0.″05, for consistency with previous work in L15.

Table 1
Preliminary Sample of SLSNe with Available HST Host Galaxy Images

		HST Image					SLSN Image	
SLSN	Redshift	Instrument	Filter	Exp. Time (s)	Obs. Date (UT)	Program ID	Telescope/Instrument	Filter
DES13S2cmm	0.663	WFC3/UVIS2	F475W	1500	2023 Feb 8	17181	Blanco/DECam	*i*
DES14C1fi	1.302	WFC3/UVIS	F606W	2500	2018 Jul 5	15303	…	…
DES14C1rhg	0.481	WFC3/UVIS	F390W	5610	2018 Aug 23	15303	Blanco/DECam	*g*
DES14S2qri	1.50	WFC3/UVIS	F625W	5576	2018 Dec 16	15303	Blanco/DECam	*i*
DES14X2byo	0.868	WFC3/UVIS	F475W	5582	2018 Feb 1	15303	Blanco/DECam	*r*
DES14X3taz	0.608	WFC3/UVIS	F390W	2456	2018 Jul 15	15303	Blanco/DECam	*z*
DES15C3hav	0.392	WFC3/UVIS	F336W	2480	2018 Feb 25	15303	…	…
DES15E2mlf	1.861	WFC3/UVIS	F775W	2564	2017 Nov 22	15303	Blanco/DECam	*i*
DES15S1nog	0.565	WFC3/UVIS	F390W	2456	2018 Feb 2	15303	Blanco/DECam	*i*
DES15S2nr	0.22	WFC3/UVIS	F336W	2456	2017 Dec 28	15303	Blanco/DECam	*i*
DES15X1noe	1.188	WFC3/UVIS	F555W	2476	2018 Jul 8	15303	Blanco/DECam	*i*
DES15X3hm	0.86	WFC3/UVIS	F475W	5582	2018 Feb 6	15303	Blanco/DECam	*i*
DES16C2aix	1.068	WFC3/UVIS	F555W	2500	2019 Jan 30	15303	Blanco/DECam	*i*
DES16C2nm	1.998	WFC3/UVIS	F775W	2488	2018 Sep 1	15303	Blanco/DECam	*z*
DES16C3cv	0.727	WFC3/UVIS	F390W	5610	2017 Nov 30	15303	Blanco/DECam	*z*
DES16C3dmp	0.562	WFC3/UVIS	F390W	2480	2018 Jul 03	15303	Blanco/DECam	*i*
DES16C3ggu	0.949	WFC3/UVIS	F475W	2500	2018 Aug 30	15303	…	…
iPTF13ajg	0.7403	ACS/WFC1	F555W	5290	2017 Sep 11	15140	P48/MOSAIC	*r*
iPTF13bdl	0.403	ACS/WFC1	F435W	2180	2018 Dec 29	15140	…	…
iPTF13bjz	0.271	WFC3/UVIS2	F390W	2472	2018 Apr 29	15140	P48/MOSAIC	*r*
iPTF13cjq	0.396	ACS/WFC1	F435W	2188	2017 Oct 20	15140	…	…
iPTF13dcc	0.431	ACS/WFC1	F435W	2172	2018 Jan 26	15140	P48/MOSAIC	*r*
iPTF13ehe	0.3434	WFC3/UVIS2	F390W	2804	2017 Dec 18	15140	P48/MOSAIC	*r*
iPTF14dck	0.576	ACS/WFC1	F475W	2180	2017 Sep 11	15140	…	…
iPTF14dek	0.332	WFC3/UVIS2	F390W	2476	2018 Aug 13	15140	…	…
iPTF14tb	0.942	WFC3/UVIS2	F555W	1500	2023 Jan 29	17181	P48/MOSAIC	*r*
iPTF15cyk	0.539	WFC3/UVIS2	F475W	1500	2023 Feb 12	17181	…	…
iPTF16bad	0.2467	WFC3/UVIS2	F390W	1500	2023 Jan 10	17181	…	…
PS1-10awh	0.908	ACS/WFC1	F606W	680	2013 Sep 4	13022	PS1/GPC1	*i*
PS1-10bzj	0.65	ACS/WFC	F606W	2160	2002 Nov 11	9500	PS1/GPC1	*i*
PS1-10ky	0.956	ACS/WFC1	F606W	680	2013 Dec 13	13022	PS1/GPC1	*i*
PS1-10pm	1.206	ACS/WFC1	F606W	1960	2012 Dec 10	13022	PS1/GPC1	*z*
PS1-11afv	1.407	ACS/WFC1	F606W	1960	2013 Apr 9	13022	PS1/GPC1	*i*
PS1-11aib	0.997	ACS/WFC1	F625W	1000	2013 Sep 12	12529	HST/ACS/WFC1	F625W
PS1-11ap	0.524	ACS/WFC1	F475W	2464	2013 Oct 9	13326	PS1/GPC1	*i*
PS1-11bam	1.565	ACS/WFC1	F814W	2304	2013 Oct 11	13326	PS1/GPC1	*i*
PS1-11bdn	0.738	ACS/WFC1	F475W	2200	2013 Nov 13	13326	PS1/GPC1	*g*
PS1-11tt	1.283	ACS/WFC1	F606W	1960	2012 Dec 2	13022	PS1/GPC1	*i*
PS1-12bmy	1.572	ACS/WFC1	F814W	2224	2013 Sep 17	13326	PS1/GPC1	*i*
PS1-12bqf	0.522	ACS/WFC1	F475W	2200	2013 Nov 18	13326	PS1/GPC1	*i*
PS1-14bj	0.5215	WFC3/UVIS2	F475W	1500	2023 Jan 29	17181	PS1/GPC1	*i*
PTF09as	0.186	WFC3/UVIS2	F336W	2476	2018 Jul 18	15140	P48/MOSAIC	*r*
PTF09atu	0.501	ACS/WFC1	F435W	5204	2017 Sep 11	15140	P48/MOSAIC	*r*
PTF09cnd	0.259	WFC3/UVIS	F390W	2224	2012 Nov 11	13025	P48/MOSAIC	*r*
PTF10aagc	0.207	WFC3/UVIS2	F336W	2468	2017 Oct 15	15140	P48/MOSAIC	*r*
PTF10bfz	0.169	WFC3/UVIS2	F336W	2468	2018 Apr 25	15140	P48/MOSAIC	*r*
PTF10bjp	0.359	WFC3/UVIS2	F390W	2804	2017 Dec 29	15140	P48/MOSAIC	*r*
PTF10hgi	0.098	WFC3/UVIS2	F336W	5570	2018 Sep 22	15140	P48/MOSAIC	*r*
PTF10nmn	0.124	WFC3/UVIS2	F336W	2456	2018 Feb 23	15140	P48/MOSAIC	*r*
PTF10uhf	0.2882	WFC3/UVIS2	F390W	2600	2018 Aug 19	15140	P48/MOSAIC	*r*
PTF10vqv	0.452	ACS/WFC1	F435W	2172	2018 Jan 11	15140	P48/MOSAIC	*r*
PTF11hrq	0.057	WFC3/UVIS2	F336W	920	2014 Nov 14	13858	P48/MOSAIC	*r*
PTF12dam	0.108	WFC3/UVIS2	F336W	984	2014 Oct 16	13858	P48/MOSAIC	*r*
PTF12gty	0.177	WFC3/UVIS2	F336W	2468	2018 Jul 3	15140	P48/MOSAIC	*r*
PTF12hni	0.1056	WFC3/UVIS2	F336W	2456	2017 Oct 15	15140	P48/MOSAIC	*r*
PTF12mxx	0.327	WFC3/UVIS2	F390W	5622	2017 Oct 24	15140	P48/MOSAIC	*r*
SCP06F6	1.189	ACS/WFC1	F606W	8054	2013 May 23	13025	HST/ACS/WFC1	F775W
SN 2005ap	0.283	WFC3/UVIS	F390W	1804	2012 Nov 25	13025	…	…
SN 2006oz	0.396	WFC3/UVIS2	F300X	1200	2017 Sep 2	14762	…	…
SN 2007bi	0.128	WFC3/UVIS	F336W	1808	2012 Nov 27	13025	LT/RATCam	*r*
SN 2009jh	0.349	WFC3/UVIS	F390W	2044	2012 Dec 6	13480	P48/MOSAIC	*r*

Table 1
(Continued)

SLSN	Redshift	HST Image					SLSN Image	
		Instrument	Filter	Exp. Time (s)	Obs. Date (UT)	Program ID	Telescope/Instrument	Filter
SN 2010gx	0.23	WFC3/UVIS	F390W	1808	2012 Nov 22	13025	Gemini-S/GMOS	*r*
SN 2010hy	0.19	WFC3/UVIS2	F336W	5592	2017 Oct 24	15140	…	…
SN 2011ke	0.385	WFC3/UVIS	F336W	2044	2013 May 16	13025	P48/MOSAIC	*r*
SN 2011kf	0.245	WFC3/UVIS	F336W	2036	2013 Jun 29	13025	LT/RATCam	*i*
SN 2011kg	0.192	WFC3/UVIS	F336W	1804	2012 Nov 12	13025	P48/MOSAIC	*r*
SN 2011kl	0.677	WFC3/UVIS	F336W	1050	2011 Dec 20	12786	…	…
SN 2012il	0.175	WFC3/UVIS	F336W	2036	2013 Jan 2	13025	…	…
SN 2015bn	0.114	ACS/WFC1	F475W	2344	2017 Jun 1	14743	HST/ACS/WFC1	F475W
SN 2016ard	0.2025	ACS/WFC1	F775W	2120	2019 Mar 19	15496	…	…
SN 2016eay	0.1013	ACS/WFC1	F625W	2180	2019 Mar 26	15162	HST/ACS/WFC1	F625W
SN 2016inl	0.3057	ACS/WFC1	F625W	2140	2019 Jul 6	15162	HST/ACS/WFC1	F625W
SN 2016wi	0.224	WFC3/UVIS2	F390W	1500	2022 Dec 18	17181	…	…
SN 2017ens	0.1086	WFC3/UVIS2	F336W	1500	2023 Jan 20	17181	…	…
SN 2018avk	0.132	WFC3/UVIS2	F336W	1500	2023 Mar 5	17181	P48/MOSAIC	*g*
SN 2018bgv	0.0795	WFC3/UVIS2	F336W	1500	2022 Nov 16	17181	FLWO/KeplerCam	*i*
SN 2018bym	0.274	WFC3/UVIS2	F390W	1500	2022 Dec 5	17181	P48/MOSAIC	*r*
SN 2018don	0.073	WFC3/UVIS2	F275W	1200	2022 Jan 9	16657	P48/MOSAIC	*r*
SN 2018fcg	0.344	WFC3/UVIS2	F336W	1500	2022 Nov 21	17181	P48/MOSAIC	*r*
SN 2018fd	0.263	WFC3/UVIS2	F390W	1500	2023 Jan 19	17181	FLWO/KeplerCam	*i*
SN 2018ffj	0.234	WFC3/UVIS	F555W	710	2021 Sep 26	16239	P48/MOSAIC	*r*
SN 2018hpq	0.124	WFC3/UVIS2	F275W	1200	2022 Feb 17	16657	P48/MOSAIC	*r*
SN 2018hti	0.0612	WFC3/UVIS	F555W	710	2021 Oct 1	16239	P48/MOSAIC	*r*
SN 2018kyt	0.108	WFC3/UVIS2	F336W	1500	2022 Dec 5	17181	P48/MOSAIC	*g*
SN 2018lzv	0.434	WFC3/UVIS2	F438W	1500	2023 Mar 5	17181	…	…
SN 2018lzw	0.3198	WFC3/UVIS2	F390W	1500	2022 Dec 15	17181	P48/MOSAIC	*r*
SN 2019cdt	0.153	WFC3/UVIS2	F336W	1500	2023 Feb 21	17181	P48/MOSAIC	*r*
SN 2019eot	0.3057	WFC3/UVIS2	F390W	1500	2022 Dec 2	17181	P48/MOSAIC	*r*
SN 2019kcy	0.40	WFC3/UVIS2	F438W	1500	2023 Jan 20	17181	P48/MOSAIC	*g*
SN 2019lsq	0.14	WFC3/UVIS2	F336W	1500	2023 Jan 6	17181	P48/MOSAIC	*r*
SN 2019neq	0.1059	WFC3/UVIS2	F336W	1500	2023 Feb 19	17181	P48/MOSAIC	*r*
SN 2019nhs	0.19	WFC3/UVIS2	F336W	1500	2022 Dec 31	17181	P48/MOSAIC	*g*
SN 2019sgh	0.344	WFC3/UVIS2	F390W	1500	2022 Nov 19	17181	FLWO/KeplerCam	*i*
SN 2019stc	0.117	WFC3/UVIS2	F336W	1500	2022 Dec 9	17181	MMT/Binospec	*i*
SN 2019ujb	0.1647	WFC3/UVIS2	F336W	1500	2023 Feb 4	17181	FLWO/KeplerCam	*i*
SN 2019unb	0.0635	WFC3/UVIS2	F275W	1200	2022 Jan 25	16657	P48/MOSAIC	*r*
SN 2019xaq	0.20	WFC3/UVIS2	F336W	1500	2023 Jan 13	17181	P48/MOSAIC	*r*
SN 2019zbv	0.37	WFC3/UVIS2	F438W	1500	2022 Dec 18	17181	FLWO/KeplerCam	*i*
SN 2019zeu	0.39	WFC3/UVIS2	F438W	1500	2023 Feb 4	17181	FLWO/KeplerCam	*i*
SN 2020ank	0.2485	WFC3/UVIS2	F390W	1500	2022 Dec 9	17181	P48/MOSAIC	*r*
SN 2020jhm	0.05	WFC3/UVIS2	F336W	1500	2022 Dec 7	17181	P48/MOSAIC	*i*
SN 2020onb	0.153	WFC3/UVIS2	F336W	1500	2023 Jan 20	17181	P48/MOSAIC	*i*
SN 2020qef	0.183	WFC3/UVIS2	F336W	1500	2023 Jan 4	17181	P48/MOSAIC	*r*
SN 2020qlb	0.1585	WFC3/UVIS2	F336W	1600	2022 Jan 7	16657	P48/MOSAIC	*r*
SN 2020rmv	0.27	WFC3/UVIS2	F336W	1600	2021 Dec 4	16657	P48/MOSAIC	*r*
SN 2020tcw	0.064	WFC3/UVIS2	F275W	1200	2022 Jun 12	16657	P48/MOSAIC	*r*
SN 2020xgd	0.454	WFC3/UVIS2	F438W	1500	2022 Dec 30	17181	P48/MOSAIC	*r*
SN 2020znr	0.10	WFC3/UVIS2	F336W	1500	2022 Dec 9	17181	Magellan/IMACS	*i*
SNLS07D2bv	1.50	ACS/WFC	F850LP	2169	2015 Mar 14	13641	…	…

Note. List of all SLSNe with archival HST host galaxy observations. We also report the telescope/instrument and filter for the events with available SN imaging used for astrometric matching.

2.2. *SLSN Imaging*

Precisely locating each SLSN within its host galaxy requires relative astrometry and hence images of the SLSN. We use the deepest, highest resolution optical images available. Specifically, we use Pan-STARRS1 Medium Deep Survey (PS1-MDS; Chambers et al. 2016) nightly stacks; Palomar Transient Factory (PTF; Rau et al. 2009; PTF Team 2020) and Zwicky Transient Facility (ZTF; Bellm et al. 2019; IRSA 2022) images accessed through the NASA Infrared Processing and Analysis Center Infrared Science Archive;[8] and Dark Energy Survey (DES; Dark Energy Survey Collaboration 2005, 2016) images accessed through NSF's NOIRLab Astro Data Lab.[9] In

[8] https://irsa.ipac.caltech.edu/
[9] https://noirlab.edu/public/projects/astrodatalab/

Table 2
SLSN Sample with HST Data

Criterion	Number of Events
Preliminary sample	109
Available SN image	95
Successful astrometric match	84
Host galaxy detected	65

addition, we also search for images on the Gemini Observatory archive[10] and the 2 m Liverpool Telescope (Steele et al. 2004) data archive.[11] Finally, in some cases, we use our own data from the 1.2 m telescope at Fred L. Whipple Observatory (KeplerCam), the 6.5 m Magellan telescopes (IMACS), and the 6.5 m MMT (Binospec).

Five SLSNe in our sample have multiple HST epochs available, which include detections of the SNe themselves. As previously analyzed in L15, the constant F625W flux and F625W – F775W color in the two final epochs of PS1-11aib (220 and 350 rest-frame days past peak) indicate no residual SN emission in the final epoch. Similarly, SCP06F6 and SN 2016eay both have HST observations taken significantly far apart (≈1170 and ≈1130 rest-frame days past peak, respectively) to rule out confidently the possibility of residual SN emission in the final epochs. We use the first epoch of HST observations of PS1-11aib, SCP06F6, and SN 2016eay as the SN images, performing image subtraction to ensure that host galaxy light does not affect the SN centroid determination. We use `PyZOGY`[12] (Zackay et al. 2016) after aligning the different HST images with our astrometry procedure (see Section 2.3).

On the other hand, for SN 2015bn and SN 2016inl, all available HST observations contain SN emission, and we therefore disentangle the SN and host galaxy contributions using `galfit` (Peng et al. 2010). For SN 2015bn, we use the Sérsic profile model from Nicholl et al. (2018) and use the host-subtracted image containing only SN light to calculate the centroid location. In the case of SN 2016inl, we use the model from Blanchard et al. (2021), where the SN and its host galaxy were simultaneously fit with a PSF and a Sérsic profile. Since the `galfit` models do not include positional uncertainties, we take the centroid locations given by `galfit` and measure the SN positional uncertainty in the same fashion as the rest of our sample and assume a typical host positional uncertainty of $\sigma_{\rm host} = 0\farcs005$ for smoothly varying galaxies in the sample (e.g., PS1-10bzj and PS1-11ap). We note that for these two SLSNe we can measure an offset, but due to the blending of SN and host galaxy light we cannot reliably determine the fractional flux statistic (see Section 3).

Taking into account the availability of SLSN images (ground based and HST), the sample size is reduced to 95 SLSNe; we do not find any publicly available SN images for the remaining 14 events; see Table 2.

2.3. Astrometry

We perform relative astrometry when possible, and absolute astrometry otherwise, on the 95 HST images with available SN images, to align and precisely locate each SLSN relative to its host galaxy.

We identify common point-like sources between the SN and HST images with `photutils` (Bradley et al. 2022) and measure the position of each source. We then match the sources using the function `wcs.fit_wcs_from_points` in `astropy` to fit a simple imaging polynomial of degree 1–3 (depending on the number of common sources) to align the SN images to the world coordinate system of the HST images. We measure the rms of the positional residuals for the common sources as the 1σ astrometric tie uncertainty, $\sigma_{\rm tie}$. We require a minimum of four common sources for a reliable fit, which is satisfied for 66 of the 95 SLSNe. For the remaining 29 events we instead use absolute astrometry by matching both the SN and the HST images to the Gaia DR3 catalog (Gaia Collaboration et al. 2016, 2023). The rms positional residuals from each fit are then combined in quadrature to determine $\sigma_{\rm tie}$.

For the sources aligned with relative astrometry, we find a median value of $\sigma_{\rm tie} \approx 33$ mas. For sources aligned with absolute astrometry, the combined tie uncertainty is somewhat higher, with a median value of $\sigma_{\rm tie} \approx 87$ mas. The number of common sources used in the astrometric matching and the resulting values of $\sigma_{\rm tie}$ are listed in Table 3. We note that for 11 sources, there is a lack of point-like sources in the HST images, rendering an astrometric match impossible. The sample size after astrometric alignment is reduced to 84 SLSNe; see Table 2.

3. Measurement Methodology

3.1. Host Galaxy Assignment

Before offsets and fractional flux values can be determined, we need to associate a host galaxy to each SLSN. We assign the most probable host galaxy for each SLSN by calculating the probability of chance coincidence ($P_{\rm cc}$) for galaxies in the vicinity of the SN location, specifically focusing on a region of 30×30 kpc. For context, the largest projected physical offsets measured in L15 was 4.3 kpc, and the offsets measured in this work are well contained within this field of view.

Following the methodology of Bloom et al. (2002; also used by Berger 2010; Fong & Berger 2013; B16), we calculate $P_{\rm cc}$ for each galaxy using:

$$P_{\rm cc} = 1 - e^{-\pi R_e^2 \sigma(\leqslant m)}, \quad (1)$$

where $\sigma(\leqslant m)$ is the observed surface density of galaxies brighter than magnitude m and R_e is the effective radius, defined as $R_e = \max(3\sqrt{\sigma_{\rm tie}^2 + \sigma_{\rm SN}^2}, \sqrt{R^2 + 4R_{50}^2})$ (Bloom et al. 2002), where R is the projected offset and R_{50} is the half-light radius (see Section 3.2). For about two-thirds of our sample, the localizations are sufficiently precise such that the second term dominates.

For each HST image, we use `photutils` to detect extended sources that are potential host candidates. To avoid spurious associations with noise fluctuations, we consider sources with a minimum of 10 connected pixels detected at $\geqslant 2.5\sigma$ above the background level. If the object with the lowest $P_{\rm cc}$ exceeds a threshold value of 0.1, we consider the actual host galaxy to be undetected at the limit of our images, and exclude the source from subsequent analysis; this is the case for 19 of the 84 sources with successful astrometric matching.

In addition to calculating $P_{\rm cc}$, we also compare our most probable host galaxy assignment with previous studies that have identified SLSN hosts (L15; Angus et al. 2016; Perley et al. 2016; Cikota et al. 2017; Schulze et al. 2018; Angus et al. 2019; Taggart & Perley 2021). We find that our assignments

[10] https://archive.gemini.edu/searchform
[11] https://telescope.livjm.ac.uk
[12] https://github.com/dguevel/PyZOGY

Table 3
Astrometric Results and Key Measurements

SLSN	# Tie Objects	$\sigma_{\rm tie}$ (arcsec)	$\sigma_{\rm SN}$ (arcsec)	$\sigma_{\rm host}$ (arcsec)	$R_{\rm phy}$ (kpc)	R_{50} (kpc)	$R_{\rm norm}$ ($R_{\rm phy}/R_{50}$)	Light Fraction	AB Mag[a]	$P_{\rm cc}$
SN 2020jhm	4	0.033	0.011	0.008	$0.724^{+0.037}_{-0.037}$	0.352	$2.056^{+0.104}_{-0.104}$	$0.000^{+0.000}_{-0.000}$	$22.632^{+0.036}_{-0.036}$	0.006
SN 2018hti	6	0.055	0.013	0.010	$0.513^{+0.070}_{-0.070}$	0.956	$0.537^{+0.074}_{-0.074}$	$0.599^{+0.075}_{-0.331}$	$19.063^{+0.006}_{-0.006}$	0.002
SN 2020tcw	5	0.094	0.010	0.007	$1.230^{+0.120}_{-0.120}$	0.553	$2.224^{+0.218}_{-0.218}$	$0.000^{+0.023}_{-0.000}$	$19.206^{+0.004}_{-0.004}$	0.001
PTF10hgi	8	0.067	0.016	0.011	$0.268^{+0.131}_{-0.131}$	0.426	$0.628^{+0.308}_{-0.308}$	$0.250^{+0.464}_{-0.250}$	$24.398^{+0.028}_{-0.028}$	0.006
SN 2020znr	24	0.018	0.001	0.002	$0.183^{+0.035}_{-0.035}$	0.104	$1.766^{+0.335}_{-0.335}$	$0.222^{+0.129}_{-0.183}$	$23.042^{+0.016}_{-0.016}$	<0.001
SN 2016eay	13	0.005	0.008	0.008	$0.072^{+0.024}_{-0.024}$	0.399	$0.180^{+0.059}_{-0.059}$	$0.924^{+0.067}_{-0.012}$	$21.983^{+0.005}_{-0.005}$	0.001
PTF12hni[b]	12, 5	0.047	0.032	<0.001	$2.667^{+0.114}_{-0.114}$	2.811	$0.949^{+0.041}_{-0.041}$	$0.000^{+0.205}_{-0.000}$	$20.320^{+0.011}_{-0.011}$	0.010
SN 2019neq	5	0.047	0.014	0.007	$0.426^{+0.099}_{-0.099}$	0.213	$2.005^{+0.468}_{-0.468}$	$0.034^{+0.289}_{-0.034}$	$23.170^{+0.024}_{-0.024}$	0.001
PTF12dam[b]	8, 4	0.091	0.008	0.008	$0.571^{+0.187}_{-0.187}$	0.665	$0.858^{+0.281}_{-0.281}$	$0.900^{+0.063}_{-0.116}$	$19.977^{+0.007}_{-0.007}$	<0.001
SN 2018kyt[b]	8, 3	0.093	0.041	0.012	$0.864^{+0.209}_{-0.209}$	0.804	$1.075^{+0.260}_{-0.260}$	$0.180^{+0.319}_{-0.180}$	$21.644^{+0.015}_{-0.015}$	0.002
SN 2015bn[c]	…	…	0.014	0.005	$0.462^{+0.031}_{-0.031}$	0.517	$0.894^{+0.061}_{-0.061}$	…	…	…
SN 2019stc	52	0.016	0.006	0.007	$0.093^{+0.040}_{-0.040}$	0.637	$0.146^{+0.063}_{-0.063}$	$0.808^{+0.052}_{-0.232}$	$22.637^{+0.029}_{-0.029}$	0.002
SN 2007bi	7	0.037	0.008	0.003	$0.183^{+0.089}_{-0.089}$	0.189	$0.971^{+0.469}_{-0.469}$	$0.144^{+0.566}_{-0.144}$	$25.245^{+0.069}_{-0.069}$	0.001
SN 2018avk[b]	6, 3	0.052	0.081	0.007	$0.187^{+0.234}_{-0.187}$	0.249	$0.748^{+0.940}_{-0.748}$	$0.418^{+0.344}_{-0.418}$	$24.117^{+0.041}_{-0.041}$	0.001
SN 2011ke	4	0.059	0.012	0.004	$0.481^{+0.157}_{-0.157}$	0.395	$1.216^{+0.398}_{-0.398}$	$0.431^{+0.214}_{-0.248}$	$22.861^{+0.016}_{-0.016}$	0.001
SN 2020qlb	10	0.028	0.013	<0.001	$0.719^{+0.087}_{-0.087}$	0.938	$0.767^{+0.093}_{-0.093}$	$0.780^{+0.174}_{-0.190}$	$22.642^{+0.019}_{-0.019}$	0.003
SN 2019ujb	6	0.037	0.036	0.008	$1.510^{+0.152}_{-0.152}$	0.566	$2.667^{+0.268}_{-0.268}$	$0.000^{+0.212}_{-0.000}$	$24.048^{+0.080}_{-0.080}$	0.007
PTF12gty	6	0.039	0.095	0.005	$0.169^{+0.317}_{-0.169}$	0.243	$0.693^{+1.301}_{-0.693}$	$0.394^{+0.399}_{-0.394}$	$26.030^{+0.098}_{-0.098}$	0.008
SN 2020qef	12	0.043	0.080	0.015	$4.044^{+0.292}_{-0.292}$	1.102	$3.670^{+0.265}_{-0.265}$	$0.000^{+0.000}_{-0.000}$	$22.575^{+0.025}_{-0.025}$	0.012
PTF09as[b]	12, 4	0.148	0.122	0.006	$0.700^{+0.618}_{-0.618}$	0.546	$1.282^{+1.132}_{-1.132}$	$0.164^{+0.271}_{-0.164}$	$23.269^{+0.018}_{-0.018}$	0.003
SN 2019nhs	4	0.054	0.042	0.004	$0.386^{+0.226}_{-0.226}$	0.139	$2.785^{+1.626}_{-1.626}$	$0.000^{+0.012}_{-0.000}$	$25.664^{+0.083}_{-0.083}$	0.003
PTF10aagc	4	0.047	0.062	0.005	$2.515^{+0.271}_{-0.271}$	1.415	$1.778^{+0.192}_{-0.192}$	$0.000^{+0.053}_{-0.000}$	$22.980^{+0.029}_{-0.029}$	0.009
SN 2010gx[b]	5, 8	0.090	0.001	0.008	$0.738^{+0.344}_{-0.344}$	0.455	$1.623^{+0.757}_{-0.757}$	$0.004^{+0.231}_{-0.004}$	$23.823^{+0.021}_{-0.021}$	0.001
SN 2018ffj[b]	8, 5	0.071	0.048	0.001	$0.586^{+0.329}_{-0.329}$	0.562	$1.043^{+0.585}_{-0.585}$	$0.444^{+0.116}_{-0.250}$	$23.343^{+0.020}_{-0.020}$	0.001
SN 2011kf	4	0.022	0.055	0.006	$0.378^{+0.238}_{-0.238}$	0.460	$0.823^{+0.519}_{-0.519}$	$0.000^{+0.356}_{-0.000}$	$25.197^{+0.067}_{-0.067}$	0.002
PTF09cnd	5	0.012	0.029	0.009	$0.375^{+0.134}_{-0.134}$	0.914	$0.410^{+0.146}_{-0.146}$	$0.558^{+0.112}_{-0.186}$	$23.915^{+0.023}_{-0.023}$	0.003
SN 2018fd[b]	8, 10	0.084	0.064	0.005	$0.179^{+0.443}_{-0.179}$	0.393	$0.454^{+1.128}_{-0.454}$	$0.712^{+0.192}_{-0.237}$	$24.216^{+0.025}_{-0.025}$	0.002
iPTF13bjz	4	0.036	0.088	0.012	$3.194^{+0.412}_{-0.412}$	0.604	$5.285^{+0.681}_{-0.681}$	$0.000^{+0.012}_{-0.000}$	$24.608^{+0.028}_{-0.028}$	0.016
SN 2018bym	17	0.034	0.027	0.007	$1.035^{+0.191}_{-0.191}$	0.531	$1.949^{+0.360}_{-0.360}$	$0.000^{+0.000}_{-0.000}$	$24.933^{+0.055}_{-0.055}$	0.004
PTF10uhf	6	0.097	0.080	0.008	$0.876^{+0.564}_{-0.564}$	8.613	$0.102^{+0.066}_{-0.066}$	$0.677^{+0.230}_{-0.269}$	$20.180^{+0.006}_{-0.006}$	0.012
SN 2019eot	10	0.026	0.046	0.009	$0.361^{+0.249}_{-0.249}$	0.934	$0.386^{+0.266}_{-0.266}$	$0.000^{+0.444}_{-0.000}$	$24.439^{+0.111}_{-0.111}$	0.004
SN 2016inl[c]	…	…	0.010	0.005	$1.335^{+0.051}_{-0.051}$	4.705	$0.284^{+0.011}_{-0.011}$	…	…	…
SN 2018lzw	8	0.035	0.039	0.008	$1.540^{+0.254}_{-0.254}$	0.477	$3.232^{+0.533}_{-0.533}$	$0.000^{+0.044}_{-0.000}$	$25.292^{+0.058}_{-0.058}$	0.006
PTF12mxx	10	0.039	0.083	0.005	$1.715^{+0.452}_{-0.452}$	1.882	$0.911^{+0.240}_{-0.240}$	$0.000^{+0.097}_{-0.000}$	$24.951^{+0.038}_{-0.038}$	0.024
iPTF13ehe	10	0.073	0.192	0.013	$3.179^{+1.035}_{-1.035}$	0.810	$3.926^{+1.279}_{-1.279}$	$0.000^{+0.244}_{-0.000}$	$25.235^{+0.042}_{-0.042}$	0.022
SN 2018fcg	29	0.087	0.050	0.026	$1.803^{+0.522}_{-0.522}$	0.859	$2.099^{+0.608}_{-0.608}$	$0.000^{+0.009}_{-0.000}$	$22.720^{+0.032}_{-0.032}$	0.002
SN 2019sgh[b]	13, 13	0.075	0.110	0.005	$1.203^{+0.671}_{-0.671}$	0.383	$3.142^{+1.753}_{-1.753}$	$0.000^{+0.160}_{-0.000}$	$24.960^{+0.046}_{-0.046}$	0.006
PTF10bjp[b]	20, 4	0.150	0.143	0.003	$1.336^{+1.073}_{-1.073}$	1.224	$1.091^{+0.877}_{-0.877}$	$0.000^{+0.272}_{-0.000}$	$23.835^{+0.021}_{-0.021}$	0.006
iPTF13dcc	4	0.057	0.106	0.011	$0.661^{+0.700}_{-0.661}$	0.582	$1.135^{+1.203}_{-1.135}$	$0.007^{+0.519}_{-0.007}$	$26.018^{+0.066}_{-0.066}$	0.011
PTF10vqv	5	0.027	0.077	0.011	$2.419^{+0.492}_{-0.492}$	1.507	$1.605^{+0.326}_{-0.326}$	$0.000^{+0.000}_{-0.000}$	$23.804^{+0.018}_{-0.018}$	0.006
PTF09atu	10	0.069	0.076	0.007	$1.111^{+0.650}_{-0.650}$	0.512	$2.170^{+1.269}_{-1.269}$	$0.000^{+0.154}_{-0.000}$	$27.566^{+0.104}_{-0.104}$	0.024
PS1-14bj	6	0.052	0.052	0.012	$2.620^{+0.477}_{-0.477}$	1.630	$1.607^{+0.293}_{-0.293}$	$0.049^{+0.547}_{-0.049}$	$25.012^{+0.080}_{-0.080}$	0.014
PS1-12bqf	18	0.024	0.017	0.022	$3.359^{+0.235}_{-0.235}$	3.330	$1.009^{+0.071}_{-0.071}$	$0.650^{+0.114}_{-0.300}$	$22.946^{+0.012}_{-0.012}$	0.009
PS1-11ap	14	0.038	0.004	0.007	$0.403^{+0.251}_{-0.251}$	0.869	$0.464^{+0.288}_{-0.288}$	$0.899^{+0.057}_{-0.133}$	$24.151^{+0.011}_{-0.011}$	0.001
DES16C3dmp	15	0.017	0.017	0.002	$0.154^{+0.164}_{-0.154}$	0.612	$0.252^{+0.267}_{-0.252}$	$0.764^{+0.105}_{-0.164}$	$22.963^{+0.008}_{-0.008}$	<0.001
DES15S1nog	12	0.020	0.016	0.005	$0.208^{+0.173}_{-0.173}$	2.275	$0.092^{+0.076}_{-0.076}$	$0.544^{+0.343}_{-0.350}$	$23.862^{+0.027}_{-0.027}$	0.007
DES14X3taz	6	0.015	0.051	0.010	$0.583^{+0.375}_{-0.375}$	0.759	$0.767^{+0.494}_{-0.494}$	$0.099^{+0.483}_{-0.099}$	$25.882^{+0.068}_{-0.068}$	0.004
PS1-10bzj	28	0.040	0.023	0.001	$0.867^{+0.329}_{-0.329}$	0.581	$1.491^{+0.567}_{-0.567}$	$0.292^{+0.130}_{-0.097}$	$24.157^{+0.006}_{-0.006}$	0.001
DES13S2cmm	19	0.047	0.030	0.005	$3.778^{+0.404}_{-0.404}$	3.031	$1.246^{+0.133}_{-0.133}$	$0.000^{+0.000}_{-0.000}$	$23.897^{+0.044}_{-0.044}$	0.015
PS1-11bdn	5	0.023	0.007	0.003	$0.428^{+0.183}_{-0.183}$	1.278	$0.335^{+0.143}_{-0.143}$	$0.824^{+0.075}_{-0.354}$	$25.971^{+0.058}_{-0.058}$	0.008
iPTF13ajg	6	0.059	0.145	0.018	$2.274^{+1.187}_{-1.187}$	0.884	$2.571^{+1.342}_{-1.342}$	$0.000^{+0.000}_{-0.000}$	$27.515^{+0.113}_{-0.113}$	0.049
DES15X3hm	18	0.029	0.010	0.006	$0.309^{+0.245}_{-0.245}$	0.660	$0.468^{+0.372}_{-0.372}$	$0.616^{+0.250}_{-0.428}$	$27.027^{+0.066}_{-0.066}$	0.005
PS1-10awh	22	0.009	0.014	0.014	$0.465^{+0.171}_{-0.171}$	0.804	$0.578^{+0.213}_{-0.213}$	$0.590^{+0.317}_{-0.496}$	$26.870^{+0.120}_{-0.120}$	0.007
iPTF14tb[b]	24, 6	0.166	0.088	0.016	$6.686^{+1.529}_{-1.529}$	1.506	$4.439^{+1.015}_{-1.015}$	$0.000^{+0.000}_{-0.000}$	$26.410^{+0.044}_{-0.044}$	0.076
PS1-11aib	28	0.004	0.012	<0.001	$0.302^{+0.106}_{-0.106}$	0.259	$1.169^{+0.408}_{-0.408}$	$0.605^{+0.203}_{-0.327}$	$26.587^{+0.123}_{-0.123}$	0.001
DES16C2aix	17	0.030	0.039	0.005	$4.597^{+0.414}_{-0.414}$	2.122	$2.166^{+0.195}_{-0.195}$	$0.000^{+0.374}_{-0.000}$	$24.665^{+0.027}_{-0.027}$	0.014
DES15X1noe	11	0.012	0.059	0.006	$0.740^{+0.511}_{-0.511}$	0.688	$1.075^{+0.742}_{-0.742}$	$0.439^{+0.279}_{-0.242}$	$24.304^{+0.014}_{-0.014}$	0.001

Table 3
(Continued)

SLSN	# Tie Objects	σ_{tie} (arcsec)	σ_{SN} (arcsec)	σ_{host} (arcsec)	R_{phy} (kpc)	R_{50} (kpc)	R_{norm} (R_{phy}/R_{50})	Light Fraction	AB Mag[a]	P_{cc}
SCP06F6	17	0.011	0.019	0.002	$0.291^{+0.187}_{-0.187}$	0.557	$0.523^{+0.336}_{-0.336}$	$0.802^{+0.136}_{-0.288}$	$28.254^{+0.085}_{-0.085}$	0.007
PS1-10pm	12	0.023	0.032	0.003	$2.333^{+0.333}_{-0.333}$	2.703	$0.863^{+0.123}_{-0.123}$	$0.293^{+0.371}_{-0.249}$	$25.169^{+0.046}_{-0.046}$	0.018
PS1- 11tt	16	0.028	0.021	0.002	$0.734^{+0.305}_{-0.305}$	1.290	$0.569^{+0.237}_{-0.237}$	$0.672^{+0.186}_{-0.384}$	$26.025^{+0.043}_{-0.043}$	0.007
PS1-11afv	20	0.028	0.032	0.006	$0.994^{+0.368}_{-0.368}$	1.570	$0.633^{+0.235}_{-0.235}$	$0.761^{+0.131}_{-0.215}$	$25.465^{+0.028}_{-0.028}$	0.007
PS1-11bam	18	0.018	0.011	0.007	$3.445^{+0.194}_{-0.194}$	1.368	$2.519^{+0.142}_{-0.142}$	$0.020^{+0.122}_{-0.020}$	$23.942^{+0.014}_{-0.014}$	0.004
PS1-12bmy	10	0.011	0.040	0.004	$1.662^{+0.367}_{-0.367}$	1.574	$1.056^{+0.233}_{-0.233}$	$0.720^{+0.223}_{-0.575}$	$25.078^{+0.032}_{-0.032}$	0.006
DES15E2mlf	13	0.019	0.024	0.004	$0.085^{+0.267}_{-0.085}$	0.988	$0.086^{+0.270}_{-0.086}$	$0.910^{+0.052}_{-0.094}$	$23.464^{+0.014}_{-0.014}$	0.001
DES16C2nm	4	0.012	0.072	0.002	$4.624^{+0.623}_{-0.623}$	1.243	$3.720^{+0.501}_{-0.501}$	$0.000^{+0.132}_{-0.000}$	$25.283^{+0.067}_{-0.067}$	0.015

Notes.
[a] Corrected for Galactic extinction.
[b] Aligned with absolute astrometry using the Gaia DR3 catalog. In these cases we report the number of common sources between the Gaia DR3 catalog and the SN and HST images, respectively, in the second column.
[c] The HST images for these sources contain residual SN emission, allowing for direct astrometry without a tie to another image, but preventing a determination of the fractional flux.

are in excellent agreement with previous studies, including those with the most complex morphology (e.g., PTF12dam and PTF12hni). In seven cases,[13] we find multiple objects in the vicinity of the SLSN position, which we consider to be disjointed components of the same host galaxy (due to patchy nature of UV emission). In these instances, we combine the components to calculate all relevant host properties. For the remainder of the sample, the most probably host galaxy is either coincident with the SLSN position or the most proximal extended source.

Our final sample of detected host galaxies contains 65 events (Table 2), which is nearly four times larger than the sample analyzed in L15. The assigned host galaxies have $P_{cc} \approx 1.8 \times 10^{-4}$–$7.5 \times 10^{-2}$; see Table 3. In Figure 2 we show the drizzled HST images, along with the location and uncertainty region of each SLSN (the quadrature sum of σ_{tie} and the SN centroid uncertainty, σ_{SN}; Section 3.2), as well as the centroid and the half-light radius of each host galaxy (see Section 3.2). The drizzled HST images for SLSNe without an identified host are shown in Figure 13 in Appendix A.

3.2. Offset Measurements

Following the astrometric matching and host galaxy assignment, we determine the angular offset of each SLSN from the UV light centroid of its host galaxy. We determine the location of each SLSN by fitting the SN image with a 2D Gaussian and calculate the image centroid and its associated uncertainty, σ_{SN}, which is determined as $\theta_{FWHM}/2(S/N)$, where θ_{FWHM} is the FWHM of the 2D Gaussian and S/N is the signal-to-noise ratio of the SN detection; see Table 3.

Next, we define the host galaxy flux-weighted centroid, as determined by `photutils` for pixels designated as part of each host galaxy. Here, the statistical uncertainty on the host centroid from `photutils` potentially underestimates the systematic uncertainties due to the irregular morphology of some hosts. To address this, we estimate the positional uncertainty (σ_{host}) by varying the detection threshold from 2.5σ to the highest threshold at which the host is still detected with a step size of 0.005σ, and then taking the standard deviation of the resulting host centroid values. The resulting values of σ_{host} are listed in Table 3.

For each SLSN we measure the projected physical offset, R_{phys}, using the SN redshift, and assign an associated total uncertainty of $\sigma_{R_{phys}} = \sqrt{\sigma_{tie}^2 + \sigma_{SN}^2 + \sigma_{host}^2}$. In addition to the projected physical offset, we also normalize the offset of each SLSN by the size of its host galaxy, R_{norm}, allowing us to explore both the population itself and to compare it to other transients that may arise in galaxies with different sizes. We use `photutils` to measure the half-light radius, R_{50}, defined as the effective circular radius that encloses 50% of the total flux within the galaxy Kron aperture. Using R_{50}, the host-normalized offsets is simply given by $R_{norm} = R_{phys}/R_{50}$ (Table 3).

3.3. Fractional Flux Measurements

As in previous studies of the locations of transients in their host galaxies (Fruchter et al. 2006; Kelly et al. 2008; Prieto et al. 2008; Kelly & Kirshner 2012; L15; B16), we measure the fractional flux statistic for each SLSN following the methodology of Fruchter et al. (2006), with a refined procedure to assess the uncertainties. The fractional flux quantifies the fraction of total flux from the host galaxy that is contained in pixels fainter than the flux value at the SLSN location, thereby providing a statistic that measures the brightness of the SLSN location compared to the entire galaxy. The resulting fractional flux value lies between zero and one, where a value of one indicates the SLSN occurred in the brightest region of its host galaxy.

In previous studies, the fractional flux was measured using an area-averaged flux value centered at the transient position, with an error circle radius given by the quadrature sum of σ_{tie} and σ_{trans}. Here, we refine this procedure using a Monte Carlo approach as follows. First, we use `photutils` to extract host galaxy pixels, using a minimum of 10 connected pixels and a threshold of 1σ above the sky background. Second, exploiting the quasi-Gaussian nature of σ_{tie} and σ_{SN}, we construct a 2D Gaussian probability distribution function centered at the pixel (x_{SN}, y_{SN}) corresponding to the SLSN centroid, with a standard deviation of $\sigma = \sqrt{\sigma_{tie}^2 + \sigma_{SN}^2}$. Third, we randomly sample a pixel based on the 2D Gaussian probability distribution associated with this pixel, and use the flux value at the chosen

[13] These objects are DES13S2cmm, PS1-10pm, PS1-14bj, PTF10uhf, PTF12hni, SN 2019eot, and SN 2019ujb.

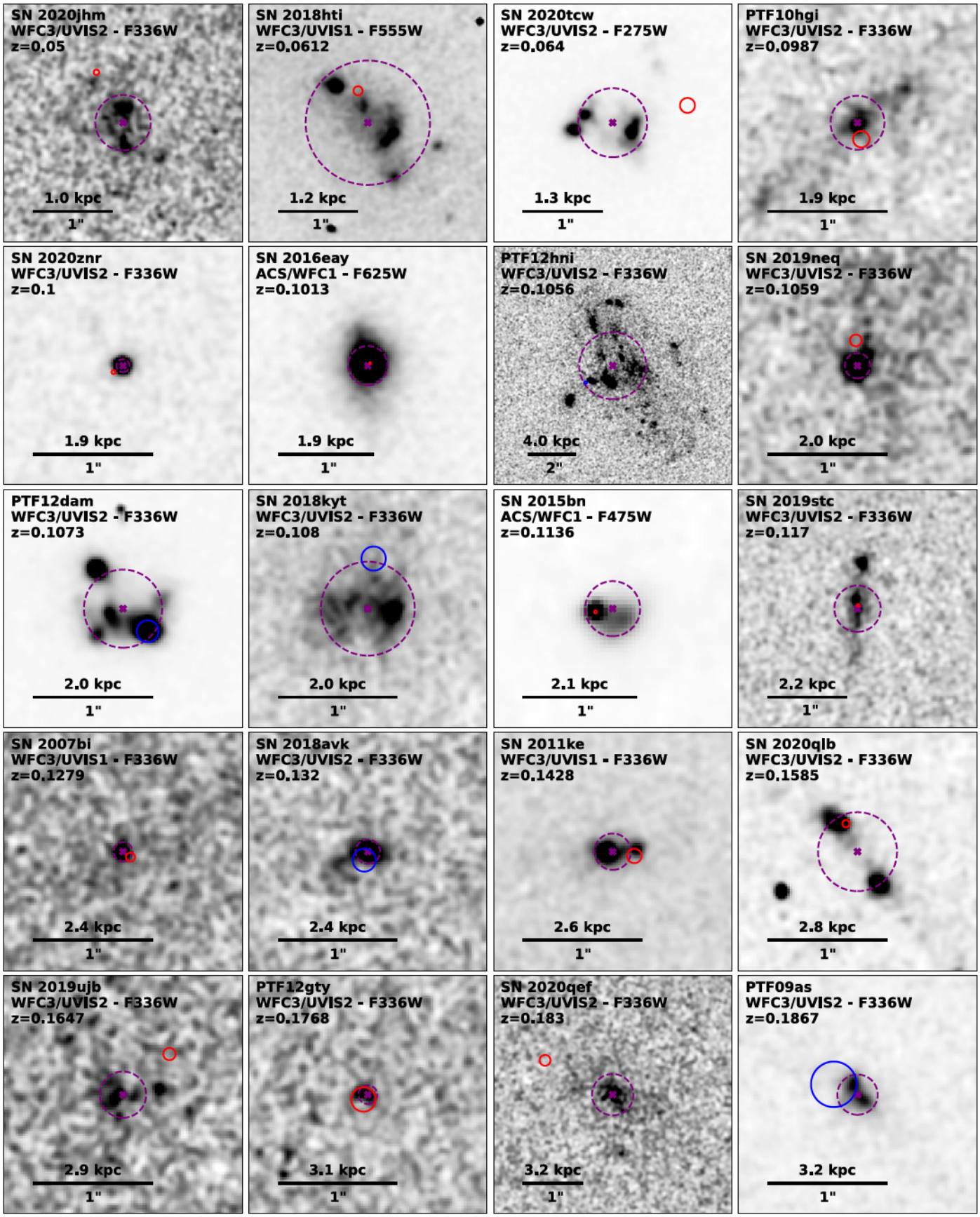

Figure 2. HST images of the 65 SLSN host galaxies with available SN imaging and successful astrometric alignment (HST images of nondetected hosts are shown in Figure 13). The images are centered on the centroid of each host galaxy (purple crosses) and aligned with north up and east to the left. The dashed purple circles marks R_{50} (half-light radius). Solid circles mark the locations of the SLSNe, with a radius corresponding to the 1σ uncertainty. Red and blue circles indicate positions determined using relative or absolute astrometry, respectively. The images have been smoothed with a 3 pixel Gaussian filter to make the host galaxies more apparent. We note that the images of SN 2015bn and SN 2016inl contain light from the SLSNe.

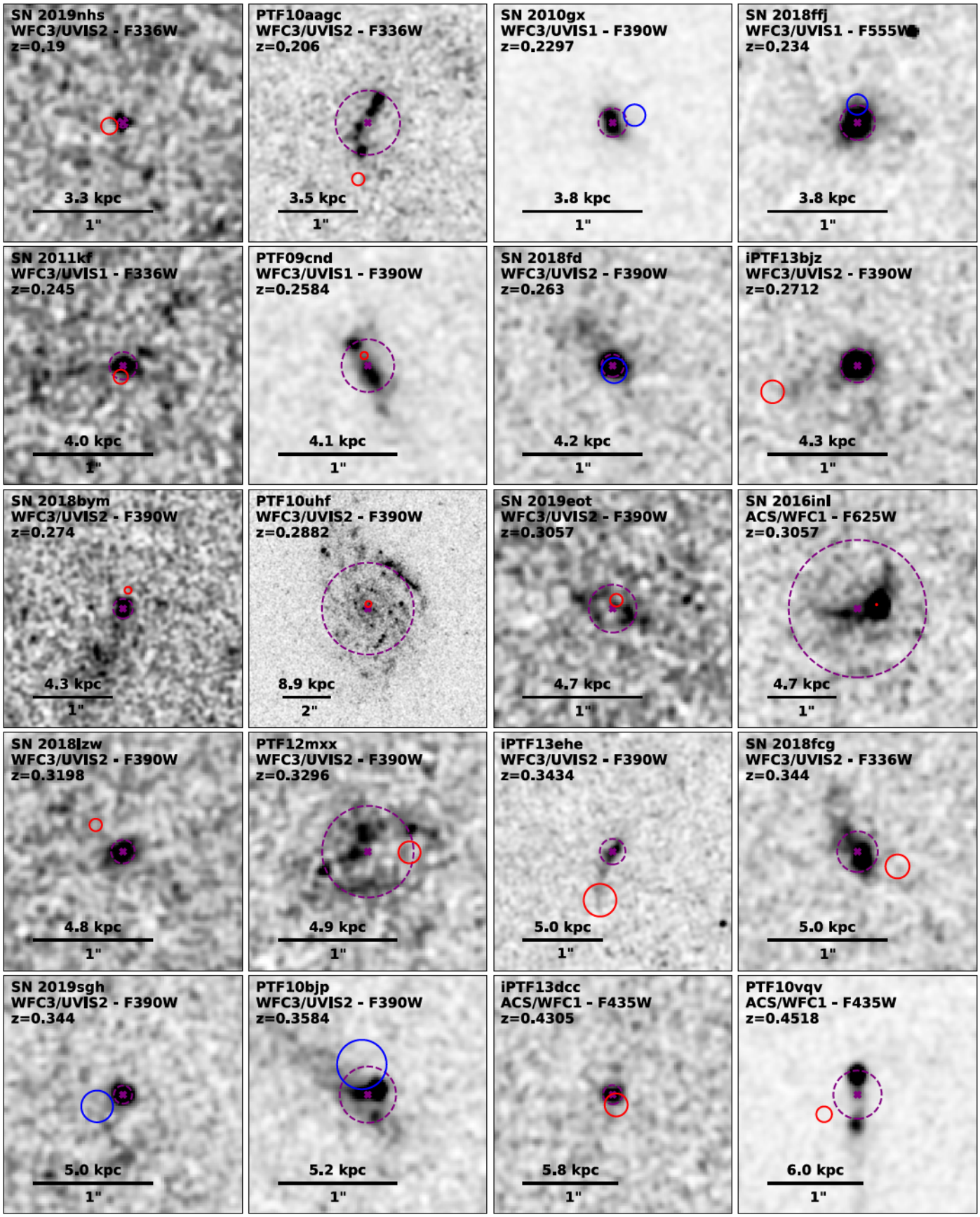

Figure 2. (Continued.)

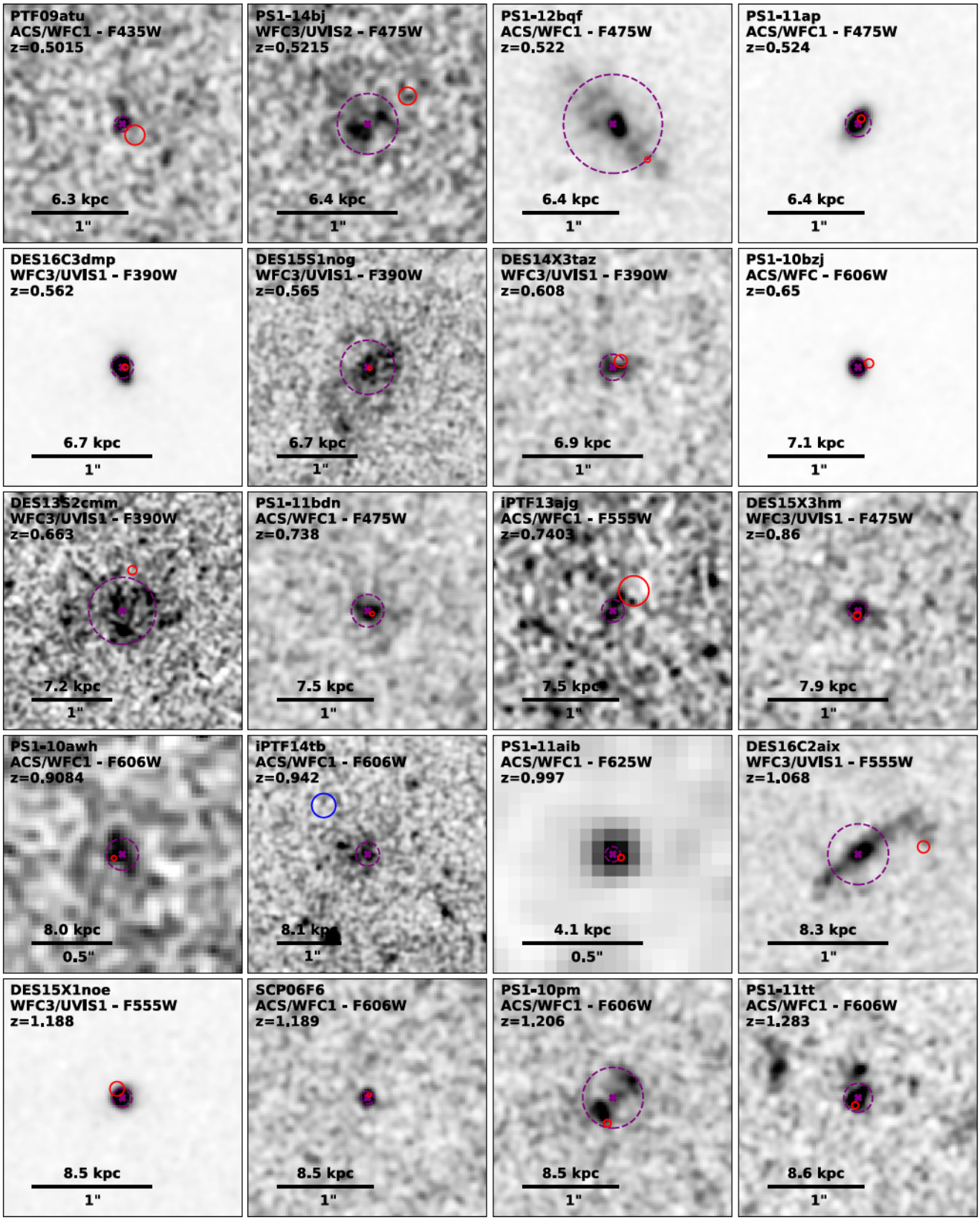

Figure 2. (Continued.)

pixel to calculate the fractional flux by dividing the sum of flux values in pixels dimmer than the chosen pixel by the total flux of the host. To determine the uncertainty on the fractional flux properly, we repeat this procedure 10,000 times. The resulting median values, as well as the 1σ ranges (corresponding to the 16th and 84th percentiles), are reported in Table 3.

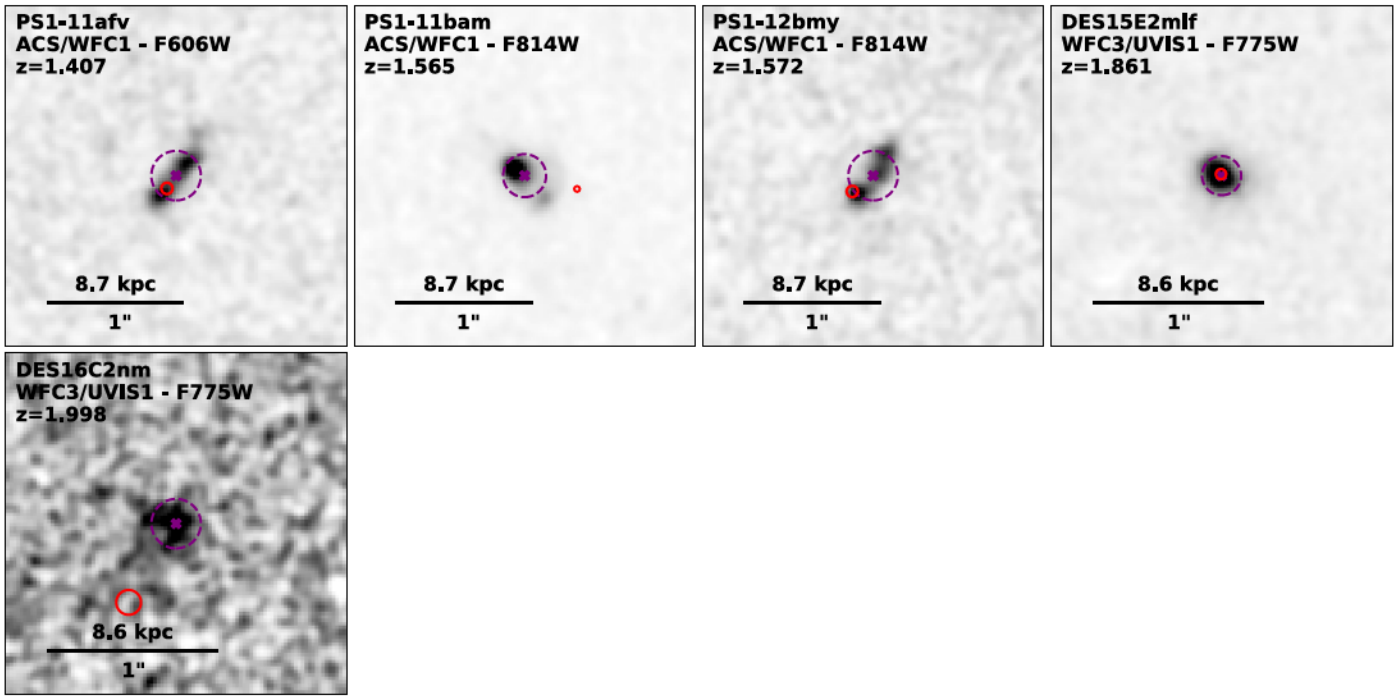

Figure 2. (Continued.)

Table 4
Summary of KS and AD Test p-values

Test	Parameter	Exp. Disk	SLSNe (L15)	LGRBs	CCSNe	SNe Ib/c	SNe II
KS	Physical offsets	⋯	0.71	0.12	⋯	2.76×10^{-11}	1.26×10^{-11}
	Host-normalized offsets	0.34	0.53	4.04×10^{-3}	⋯	1.12×10^{-3}	2.11×10^{-2}
	Fractional fluxes	⋯	1.31×10^{-2}	1.83×10^{-6}	4.61×10^{-5}	5.57×10^{-6}	5.00×10^{-6}
AD	Physical offsets	⋯	0.81	0.20	⋯	2.39×10^{-10}	3.60×10^{-17}
	Host-normalized offsets	0.17	0.45	1.17×10^{-3}	⋯	2.42×10^{-4}	1.59×10^{-2}
	Fractional fluxes	⋯	3.78×10^{-4}	1.39×10^{-10}	2.06×10^{-6}	5.23×10^{-8}	1.25×10^{-7}

Note. The comparison samples used here are SLSNe (L15), LGRBs (B16), CCSNe (Svensson et al. 2010), SNe Ib/c and II offsets (Kelly & Kirshner 2012), and SNe Ib/c and II fractional fluxes (Kelly et al. 2008).

4. Results

Our final sample of 65 SLSNe with offset and fractional flux measurements is four times larger than in the previous study of L15. In this section we describe the results from this large population, and quantitatively compare these with the distributions for other transients with massive-star progenitors (LGRBs, SNe Ib/c, and SNe II) using the Kolmogorov–Smirnov (KS; Smirnov 1948) and Anderson–Darling (AD) (Anderson & Darling 1952) tests. Both tests are designed to determine whether two distributions arise from the same underlying population, with the AD test being a modified version of the KS test that is more sensitive to the tails of a distribution (whereas the KS test gives more weight to the region around the median of a distribution). While the KS test is more widely used in previous works, we regard the AD test to be a more robust statistical measure, especially in the context of the fractional flux distribution where tail contributions are more prominent. We provide comparisons of the distributions of physical and host-normalized offsets, galaxy sizes, and fractional flux values, and summarize the KS and AD test p-values in Table 4. We stress that these statistical comparisons were severely limited by the small sample size in the previous study (L15).

4.1. Physical Offsets

In Figure 3 we show the cumulative distribution of projected physical offsets ($R_{\rm phys}$). The distribution spans ≈0.07–6.7 kpc, with a median of $\langle R_{\rm phys} \rangle \approx 0.73$ kpc. The distribution is overall smooth across the full range of offsets, with no notable gaps. The KS and AD tests comparing our distribution with the smaller sample of 16 SLSNe from L15 yield p-values of 0.71 and 0.81, respectively. This is not surprising given that the sources in the L15 sample are also included in our larger data set.

We also compare the projected physical offsets to the distributions for LGRBs from B16 as well as SNe Ib/c and II from Kelly & Kirshner (2012); see Figure 3. All three populations have systematically larger offsets than SLSNe: LGRBs by a factor 1.4, SNe Ib/c by a factor of 4.4, and SNe II by a factor of 5.5. The KS and AD tests relative to the LGRBs sample yield p-values of 0.12 and 0.20, respectively, suggesting that the physical offset distributions for SLSNe and LGRBs

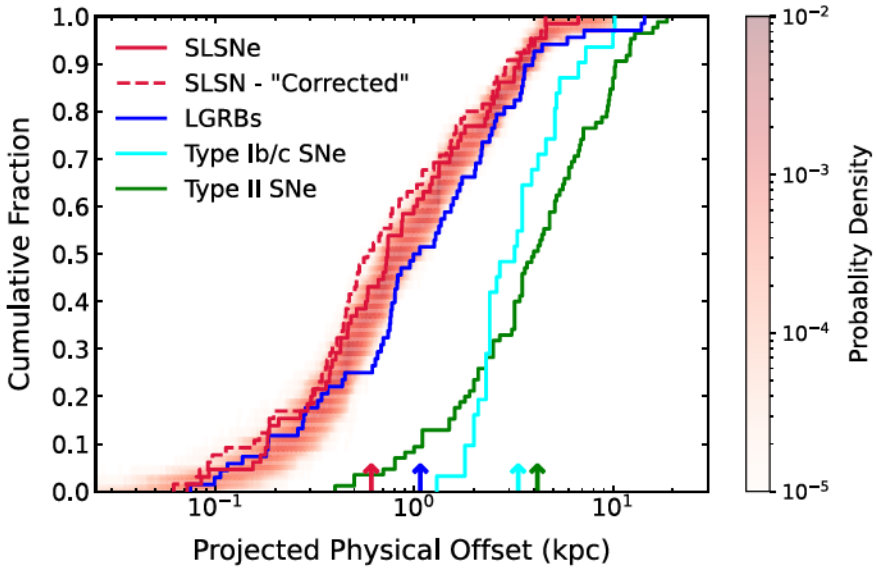

Figure 3. Cumulative distribution of projected physical offsets for 65 SLSNe from this work (red). Also shown are the distributions for LGRBs (blue; B16) and SNe Ib/c (cyan) and II (green) from Prieto et al. (2008). The red shaded region shows the results of our Monte Carlo simulation using the associated uncertainties as a 2D histogram. The arrows at the bottom denote the median of each distribution. The dashed red line includes a correction factor to account for the positive-definite nature of the offsets (see Appendix B for details).

are consistent with being drawn from the same underlying distribution. For the SNe Ib/c sample, the KS and AD tests yield p-values of 2.8×10^{-11} and 2.4×10^{-10}, respectively, while for the SNe II the p-values are 1.3×10^{-11} and 3.6×10^{-17}, respectively, thus indicating clearly that the SLSN physical offsets are vastly different from those of SNe Ib/c and II.

The offsets have associated uncertainties, $\sigma_{R_{\rm phys}}$ and $\sigma_{R_{\rm norm}}$, that are dependent on $\sigma_{\rm tie}$, $\sigma_{\rm SN}$, and $\sigma_{\rm host}$. Since the offset is a positive-definite quantity, we cannot assume a Gaussian distribution for its uncertainty. Instead, we use the Rice distribution to represent the probability distribution function (Bloom et al. 2002):

$$p(x|R,\,\sigma_R) = \frac{x}{\sigma_R^2}\exp\left[-\frac{(x+R)^2}{2\sigma_R^2}\right] I_0\left(\frac{xR}{\sigma_R^2}\right), \qquad (2)$$

where R and σ_R are the offset quantity (physical or normalized) and its uncertainty, respectively, and I_0 is the zeroth-order modified Bessel function of the first kind. Here we employ a Monte Carlo approach with 10,000 iterations to assess the uncertainties on the measured offset distributions.

Accounting for the uncertainties in the physical offsets, we show in Figure 3 the results of the Monte Carlo simulation by plotting a 2D histogram of the density of points from the cumulative distributions generated during each of the 10,000 iterations. Dark regions indicate a higher density of points, or, in other words, more synthetic distributions from the simulation pass through that region. The median of the distribution of medians from the Monte Carlo simulation is 0.81 kpc with a 90% confidence interval of 0.71–0.97 kpc. The overall apparent shift in the Monte Carlo distribution to higher offsets compared to the median distribution is due to the fact that the offset is a positive-definite quantity. Recalculating the KS and AD tests for each iteration in comparison to LGRBs, SNe Ib/c and SNe II, we confirm the same result as above.

Due to the positive-definite nature of the offsets, offsets with large uncertainties are more likely to be skewed toward higher values. In Appendix B we explore this issue and undertake a simple procedure to correct for this potential bias. In Figure 3 we show the "corrected" distribution, but find that it overall closely matches the directly observed one. Since the correction is small, and since it was not applied for other transients to which we compare our SLSN sample, we do not use it in our analysis to prevent introducing additional bias in comparison to previous works.

4.2. Galaxy Sizes

To compare the projected offsets, both for the SLSN sample itself and in comparison to other transients, in a more meaningful way, we need to normalize each offset by the size of the host galaxy, i.e., $R_{\rm norm}$. We use R_{50}, the circular radius containing half of the galaxy light, to normalize the offsets. We show the distribution of R_{50} for SLSNe in Figure 4. We find a median value of 0.76 kpc, and an overall range of ≈0.1–8.6 kpc. We also show the R_{50} distribution for LGRBs (B16), which has a median of 1.8 kpc and a range of 0.4–5.9 kpc. Thus, SLSN hosts are on average about a factor of 2.4 times smaller than even the overall compact host galaxies of LGRBs.

The KS and AD tests between the SLSN and LGRB R_{50} distributions yield p-values of 4.1×10^{-9} and 3.2×10^{-11}, respectively, clearly indicating that the two distributions are not drawn from the same underlying population. We only compare the R_{50} distribution to LGRBs, as the values were not reported for SNe Ib/c and SNe II in Kelly & Kirshner (2012).

4.3. Host-normalized Offsets

In Figure 5 we plot the cumulative distribution of host-normalized offsets ($R_{\rm norm}$). The distribution has a median value of ≈1.06, and spans a range of ≈0.09–5.28 (with about three-quarters of the SLSNe having $R_{\rm norm} \lesssim 2$). The shaded region in Figure 5 shows the results of our Monte Carlo simulation taking into account the uncertainties on the individual measurements, as described in Section 4.1. The median of

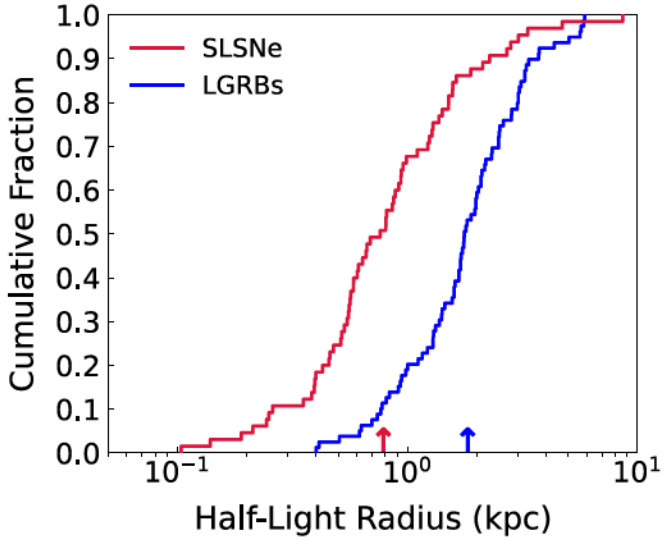

Figure 4. Cumulative distribution of host galaxy half-light radii (R_{50}) for our SLSN sample (red) and LGRBs (blue; B16). The SLSN host galaxies have a median size of $\langle R_{50}\rangle \approx 0.76$ kpc, about a factor of 2.4 times smaller than the LGBR host galaxies. We note that the R_{50} distributions for SNe Ib/c and SNe II were not reported in previous studies.

the distribution of medians is 1.17 with a 90% confidence interval of 1.01–1.35.

Overall, the distribution is reminiscent of an exponential disk profile, the expected surface brightness profile of star-forming disk galaxies, although the SLSN distribution is broader, especially at large offsets. The KS and AD tests comparing the SLSN and exponential disk distributions yield p-values of 0.34 and 0.17, respectively, indicating that the observed SLSN distribution is consistent with a smooth exponential disk distribution. Using the Monte Carlo range of cumulative distributions, we find that about 54% and 14% yield KS and AD p-values of $\gtrsim$0.05, respectively.

We also compare the SLSN host-normalized offset distribution to the distributions for LGRBs (B16) and SNe Ib/c and II (Kelly & Kirshner 2012). The LGRB and SNe Ib/c distributions have smaller medians by about a factor of 2 and 1.4, respectively, while the SNe II distribution has a comparable median value. The KS tests comparing the SLSN distribution to the three populations yield p-values of 4.1×10^{-3} (LGRBs), 1.1×10^{-3} (SNe Ib/c), and 2.1×10^{-2} (SNe II), while the AD tests yield p-values 1.2×10^{-3} (LGRBs), 2.4×10^{-4} (SNe Ib/c), and 1.6×10^{-2} (SNe II). This indicates that the SLSN host-normalized offset distribution is distinct from those of LGRBs and CCSNe, specifically extending to larger offsets.

To help visualize the comparison between the SLSNe and other transients, and each with the exponential disk, in Figure 6 we plot the difference between each cumulative distribution and the exponential disk distribution. The results illustrate that none of these transient populations strictly follow an exponential disk profile. While the SLSNe are overall consistent with an exponential disk profile, they differ from the other transient populations significantly in the way they deviate from the exponential disk distribution. Specifically, we find that the main deviation for the SLSNe is an overabundance of large normalized offsets, $R_{\rm norm} \approx 1.5$–4, while for the LGRBs there is an overabundance of small offsets, $R_{\rm norm} \approx$ 0.2–1; for the SNe Ib/c and II there is an overabundance at $R_{\rm norm} \approx 1$.

4.4. Fractional Flux Distribution

In Figure 7 we show the cumulative distribution of fractional flux for 63 SLSN host galaxies.[14] Also shown is a diagonal 1:1 line which marks the expectation of a population of sources that linearly tracks the underlying light distribution of their host galaxies. Remarkably, the SLSN sample exhibits a high fraction of events ($\sim$0.4) with a fractional flux value of 0, and has a low median value of $\approx$0.16. Thus, the locations of SLSNe appear to be significantly skewed to dimmer than average UV regions of their host galaxies. We also show the resulting 2D probability density using the Monte Carlo procedure described in Section 3.3; we still find that all 10,000 draws have a substantial fraction of $0.37^{+0.06}_{-0.08}$ (90% confidence interval) of the population with fractional flux values of 0. We note that our distribution is in tension with the smaller sample in L15, with KS and AD test p-values of 1.3×10^{-2} and 3.8×10^{-4}, respectively. Only $\sim$15% of our Monte Carlo simulations have a KS test p-value $\geqslant 0.05$, while none has an AD test p-value $\geqslant 0.05$.

The results for the SLSNe are also remarkable in comparison to the distributions for LGRBs (B16), CCSNe (Svensson et al. 2010), and SNe Ib/c and II as separate populations (Kelly et al. 2008). All of these other populations either roughly track the 1:1 line, or are skewed to brighter than average regions of their hosts, with median values of about 0.8 (LGRBs), 0.65 (SNe Ib/c), 0.6 (CCSNe), and 0.45 (SNe II); none of the comparison populations exhibit an overabundance of events with fractional flux values of zero. Formally, the KS tests between the SLSN distribution and the other distributions yield p-values of 1.8×10^{-6} (LGRBs), 4.6×10^{-5} (CCSNe), 5.6×10^{-6} (SNe Ib/c), and 5×10^{-6} (SNe II), respectively. The AD tests yield p-values of 1.4×10^{-10} (LGRBs), 2.1×10^{-6} (CCSNe), 5.2×10^{-8} (SNe Ib/c), and 1.2×10^{-7} (SNe II), respectively. None of our Monte Carlo simulations have a p-value $\geqslant 0.05$ for either test between the SLSNe and the other populations.

The overall low fractional flux values of the SLSNe compared to the other transients can most likely be attributed to the evolution of their progenitor systems, which we discuss in Section 5.3. However, there may be other factors at play that could influence the number of events with fractional flux values of zero and possibly complicate the comparison. Most notably, the depths of our images could prevent detection of the low surface brightness regions of the host galaxies. These effects are likely negligible, since additional contributions from faint pixels will not drastically increase individual fractional flux values, and the relative positions between samples are the crucial aspect when carrying out the fractional flux comparison. In this vein, Fruchter et al. (2006) experimented by artificially increasing the noise levels in their images and the detection threshold for determining galaxy pixels. Both of these procedures led to more loss of faint galaxy structures, but had minimal effects on the overall distribution for their samples. By carrying out a similar experiment, we also reach the same conclusion. We also note that the typical depth achieved in the HST images for the SLSN and LGRB samples (which would be most affected by image depth due to their wide redshift ranges) are comparable. Given the similarity between the host galaxies of SLSNe and LGRBs (compact

[14] We exclude SN 2015bn and SN 2016inl for which a measurement of the fractional flux is not possible due to the presence of SN emission in the HST images.

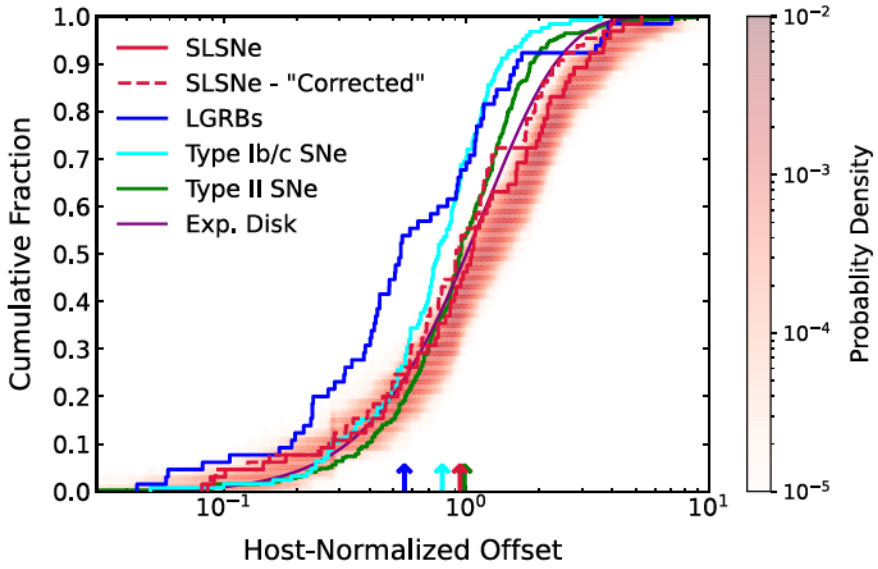

Figure 5. Cumulative distribution of host-normalized offsets for 65 SLSNe from this work (red). Also shown are the distributions for LGRBs (blue; B16) and SNe Ib/c (cyan) and II (green) SNe from Kelly & Kirshner (2012). We also plot the distribution expected for an exponential disk profile (purple). The red shaded region shows the results of our Monte Carlo simulation using the associated uncertainties as a 2D histogram. The arrows at the bottom denote the median of each distribution. The dashed red line includes a correction factor to account for the positive-definite nature of the offsets (see Appendix B for details).

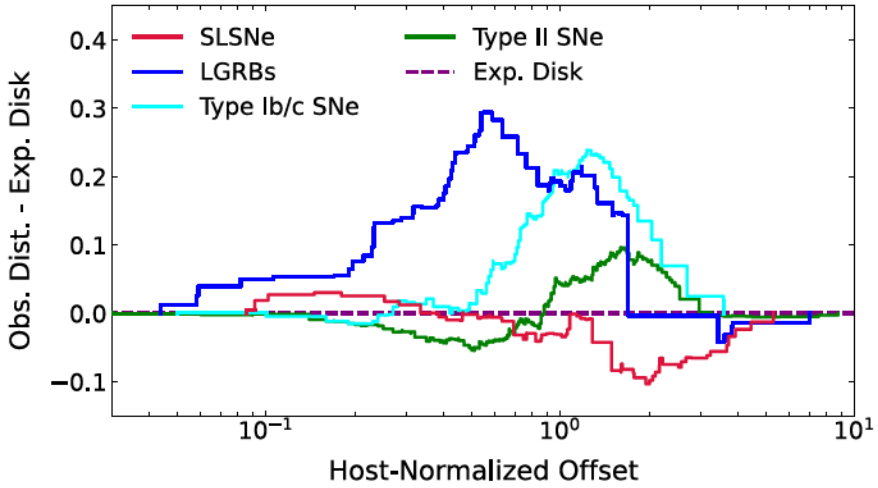

Figure 6. The differences between the cumulative host-normalized offset distributions of our SLSN sample (red), LGRBs (blue), SNe Ib/c (cyan), and SNe II (green) SNe and the cumulative distribution for an exponential disk profile. We find an overabundance of SLSNe at $R_{\rm norm} \gtrsim 1.5$, compared to an overabundance of LGRBs at $R_{\rm norm} \approx 0.2$–1 and an SNe Ib/c and II overabundance at $R_{\rm norm} \approx 1$.

dwarf galaxies), the fact that the fractional flux values of LGRBs do not exhibit significant depth-related effects only instills more confidence in our comparisons.

Another potential bias arises due to the range of spatial resolutions captured by the SLSN sample. More distant events have decreased spatial resolutions, causing blending of galaxy structures. This may skew the fractional flux to higher or lower values for higher-redshift events. However, our Monte Carlo procedure takes into account the positional uncertainties of the SN locations, which likely dominate over any resolution effect. In addition, the LGRB sample in B16 that spans an even broader redshift range does not show any redshift trends, which indicates that in practice resolution does not significantly affect the fractional flux. We therefore rule out any significant observational effects on the fractional flux distributions and the possibility that SLSNe are drawn from the same population as other transients in terms of their association with the UV light of their host galaxies.

4.5. Fractional Flux–Offset Relationship

In Figure 8 we plot fractional flux values versus host-normalized offsets for the SLSNe in our sample, LGRBs (B16), and SNe Ib/c and II (fractional fluxes: Kelly et al. 2008; normalized offsets: Kelly & Kirshner 2012). We also show the relation between fractional flux and normalized offset for an exponential disk distribution, determined by integrating the exponential disk profile at each normalized offset value. We calculate the Spearman's rank correlation coefficients (ρ; Spearman 1904) to quantify the strength of correlation between the fractional flux and normalized offset, as well as its associated 1σ bound uncertainty using the method described in Curran (2014). We find a clear negative correlation between fractional flux and normalized offset for SLSNe, with $\rho \approx -0.77$, such that sources with smaller offsets have high fractional flux values. We find similar negative correlations for the other populations ($\rho \approx -0.75$ for LGRBs, $\rho \approx -0.70$ for

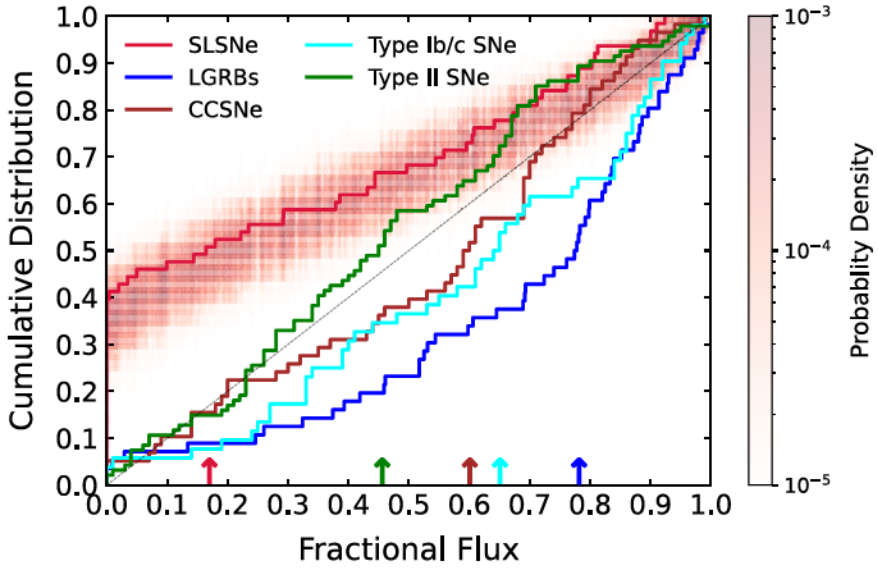

Figure 7. Cumulative distributions of fractional flux for our sample of 63 SLSNe (red; this excludes SN 2015bn and SN 2016inl). Also shown are the distributions for LGRBs (blue; B16), CCSNe (brown; Svensson et al. 2010), and SNe Ib/c (cyan) and II (green) from Kelly et al. (2008). The red shaded region indicates the 1σ uncertainty region from our Monte Carlo procedure (Section 4.4). The diagonal dashed line marks the expected fractional flux distribution for a population that uniformly traces the underlying light of their host galaxies. The arrows at the bottom denote the medians of the various distributions.

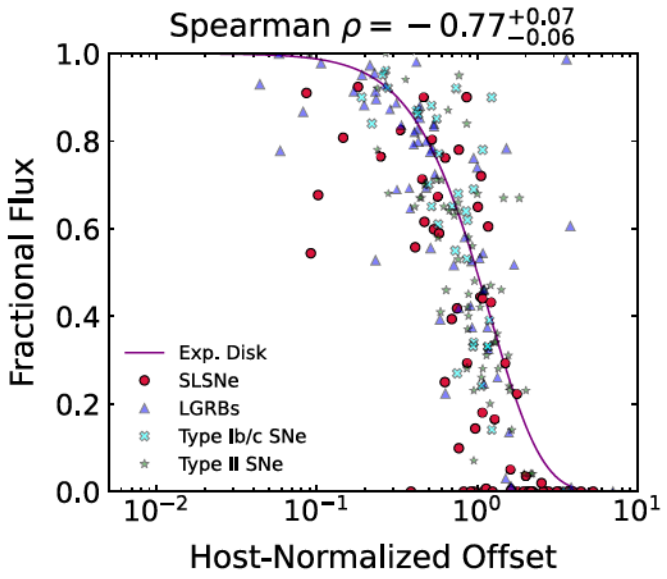

Figure 8. Scatterplots of fractional flux vs. host-normalized offsets for SLSNe (red), LGRBs (blue), SNe Ib/c (cyan), and SNe II (green), and the predicted relationship for a transient population that follows the exponential disk model exactly (purple). To avoid clutter, we omit showing the associated uncertainties on the fractional flux and host-normalized offsets. We find a strong correlation between fractional flux and host-normalized offset for SLSNe, with a median $\rho \approx -0.77$ and low uncertainties.

SNe Ib/c, and $\rho \approx -0.76$ for SNe II). Thus, all populations follow a similar trend, which overlaps well with the exponential disk profile. This trend is not surprising given that the central regions of galaxies are brighter.

However, what does stand out in the SLSN population compared to the other transients (and to an exponential disk) is the unusually large fraction of sources with fractional flux values of zero and normalized offsets of $\gtrsim 1$. These can clearly be seen along the bottom of Figure 8. To illustrate this point further, in Figure 9 we plot the cumulative fractional flux distributions for the SLSNe and the other transients, separated into subpopulations with $R_{\rm norm} \leqslant 1$ and $R_{\rm norm} > 1$. We find that SLSNe with $R_{\rm norm} \leqslant 1$ overall follow the 1:1 line expected for sources that linearly track the UV light distribution of their hosts. However, even within this subpopulation the SLSNe are somewhat more skewed to lower fractional values compared to LGRBs and SNe Ib/c and II. On the other hand, of the SLSNe with $R_{\rm norm} > 1$ about two-thirds have fractional flux values of zero, while in the other populations the fraction of such events is $\lesssim 0.15$.

5. Discussion

The distributions of offsets, fractional fluxes, and host galaxy sizes presented in Section 4 provide the most in-depth analysis of the locations and local environments of SLSNe to date. In this section we explore whether the locations of SLSNe and their host sizes exhibit trends with redshift, as well as any correlations with the inferred properties of their magnetar engines as determined from modeling of the optical light curves. We further explore implications of our results for SLSN progenitors. The Spearman's correlation coefficients are summarized in Table 5.

5.1. Trends with Redshift

In Figure 10 we plot the physical and host-normalized offsets, fractional fluxes, and host galaxy half-light radii as functions of SLSN redshift. No obvious correlation is seen between offset and redshift, with $\rho = 0.28^{+0.12}_{-0.12}$ and $\rho = -0.02^{+0.13}_{-0.12}$ for the physical and host-normalized offsets, respectively. Similarly, no obvious trend is seen between fractional flux and redshift, with $\rho = 0.13^{+0.13}_{-0.14}$. However, we find that nearly all SLSNe with low fractional flux values of $\lesssim 0.2$ are preferentially located at low redshifts, $z \lesssim 0.5$. Finally, we do find a mild correlation between host galaxy half-light radii and redshift, with $\rho = 0.49^{+0.09}_{-0.10}$, predominantly due to the prevalence of compact hosts with $R_{50} \lesssim 0.25$ kpc at $z \lesssim 0.25$.

To discern parameter trends with redshift further, in Figure 11 we present cumulative histograms split into two

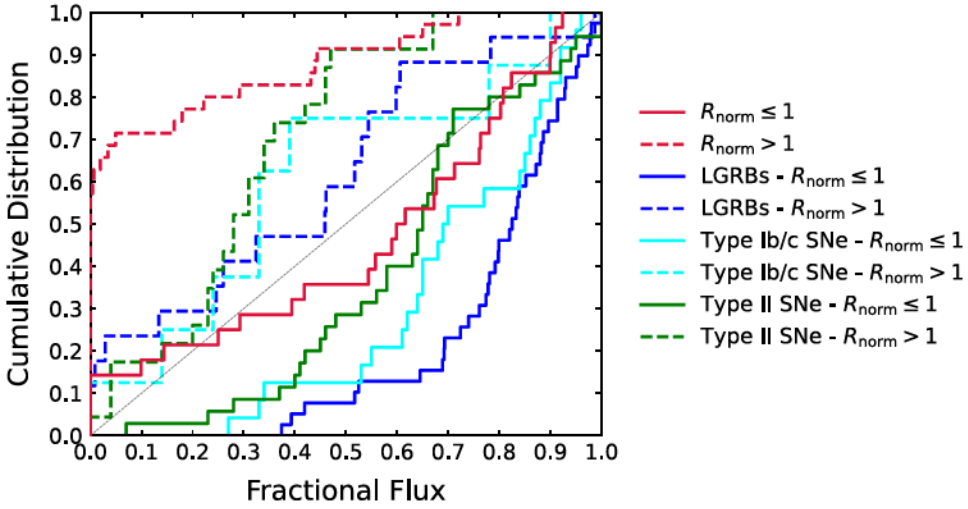

Figure 9. Same as Figure 7, but with the distributions separated into sources with $R_{\rm norm} < 1$ (solid) and $R_{\rm norm} \geqslant 1$ (dashed). The SLSN population exhibits the lowest fractional flux values in both subsets of the population, but sources with $R_{\rm norm} < 1$ roughly track the underlying UV light.

Table 5
Summary of Spearman's Rank Correlation Coefficients

Paramer	$R_{\rm phys}$	$R_{\rm norm}$	Fractional Flux	R_{50}
Redshift	$+0.28^{+0.12}_{-0.12}$	$-0.02^{+0.13}_{-0.12}$	$+0.13^{+0.13}_{-0.14}$	$+0.49^{+0.09}_{-0.10}$
Fractional flux	...	$-0.77^{+0.07}_{-0.05}$	...	...
P	$+0.16^{+0.13}_{-0.14}$	$+0.14^{+0.13}_{-0.13}$	$-0.22^{+0.13}_{-0.12}$	$+0.09^{+0.13}_{-0.13}$
B	$+0.22^{+0.12}_{-0.13}$	$+0.14^{+0.11}_{-0.12}$	$-0.27^{+0.11}_{-0.11}$	$+0.11^{+0.13}_{-0.13}$
$M_{\rm ej}$	$+0.24^{+0.11}_{-0.12}$	$-0.01^{+0.14}_{-0.14}$	$+0.11^{+0.12}_{-0.13}$	$+0.24^{+0.12}_{-0.13}$
$v_{\rm ej}$	$+0.16^{+0.13}_{-0.13}$	$-0.06^{+0.12}_{-0.11}$	$+0.01^{+0.13}_{-0.13}$	$+0.26^{+0.12}_{-0.13}$
$E_{\rm kin}$	$+0.25^{+0.13}_{-0.14}$	$-0.06^{+0.13}_{-0.13}$	$-0.11^{+0.13}_{-0.13}$	$+0.31^{+0.11}_{-0.12}$
$L_{\rm peak}$	$-0.25^{+0.15}_{-0.15}$	$-0.16^{+0.13}_{-0.13}$	$-0.28^{+0.13}_{-0.13}$	$-0.13^{+0.14}_{-0.13}$
$E_{\rm rad}$	$-0.15^{+0.14}_{-0.13}$	$-0.13^{+0.12}_{-0.12}$	$-0.32^{+0.12}_{-0.13}$	$-0.04^{+0.13}_{-0.12}$

redshift bins at $z = 0.35$ (leading to an essentially equal number of 37 and 38 SLSNe per bin). We find no clear difference in the cumulative distributions of physical offsets (KS and AD test p-values of 0.34 and 0.18, respectively) and host-normalized offsets (KS and AD test p-values of 0.53 and 0.79, respectively). We do find lower fractional flux values at $z \leqslant 0.35$ (due to the prevalence of sources with fractional flux values of zero at lower redshifts as noted above); however, the KS and AD tests yield p-values of 0.27 and 0.12, respectively, indicating no clear statistical difference. In this context, the drastic disagreement in fractional flux distributions between L15 and our sample is likely due to small number statistics and not related to any redshift effects. Finally, the only distribution that does exhibit a statistically significant trend is the half-light radius, with KS and AD test p-values of 1.4×10^{-3} and 3.5×10^{-4}, respectively, indicating that lower-redshift SLSN hosts are systematically more compact than at higher redshifts.

5.2. Trends with Magnetar Engine Parameters

The optical light curves of SLSNe have been successfully modeled with a magnetar spin-down model (Kasen & Bildsten 2010; Woosley 2010; Dessart et al. 2012; Metzger et al. 2015), in particular using `MOSFiT`[15] (Guillochon et al. 2018), an open-source, `Python`-based package that employs a Markov Chain Monte Carlo algorithm to fit a one-zone, gray-opacity analytical model to multiband light curves (Nicholl et al. 2017c; Guillochon et al. 2018). Here, we compare offset, galaxy size, and fractional flux to magnetar engine parameters to discern possible correlations between SLSN environments and power source. To ensure proper comparison with a consistent model implementation, we use the parameters from Gomez et al. (2022).

The four magnetar model parameters we use are the neutron star's initial spin period (P) and magnetic field strength (B), and the ejecta mass ($M_{\rm ej}$) and velocity ($v_{\rm ej}$); we use the latter two to also determine the kinetic energy $E_{\rm kin} = (3/10)M_{\rm ej}v_{\rm ej}^2$ of the ejecta. In addition, we also compare to the observed peak luminosity ($L_{\rm peak}$) and observed total radiated energy ($E_{\rm rad}$). In Figure 12 we plot the distributions of these seven SLSN parameters as a function of physical and normalized offsets, fractional flux, and half-light radius. Visual inspection does not reveal any significant correlation between any pair of parameters. The strongest correlation quantified by the Spearman's rank correlation coefficient is between half-light radius and kinetic energy, with a median $\rho \approx 0.31$. Thus, we find no evidence of correlation between SLSN locations and their magnetar engine or explosion properties.

5.3. Progenitor Implications

Our key finding is that SLSNe are on average located further away from their galactic centers than LGRBs and CCSNe, and unlike LGRBs and CCSNe, a substantial fraction of $\sim$40% is not strongly correlated with the underlying UV emission of their hosts. The difference relative to LGRBs is particularly intriguing given that both populations represent a rare mode of massive-star death ($\lesssim$1% of the overall CCSN rate), and both are thought to be powered by central engines that require rapid rotation (black holes in LGRBs, and magnetars in SLSNe). Our results, however, indicate that they arise from massive stars that reside in different environments.

Since a strong correlation with bright UV regions, as is the case for LGRBs, can be interpreted as evidence for a particularly young and massive progenitor population (e.g., Fruchter et al. 2006; Kelly et al. 2008; Anderson et al. 2012), the results for SLSNe may be evidence for less-massive and

[15] https://mosfit.readthedocs.io/en/latest/

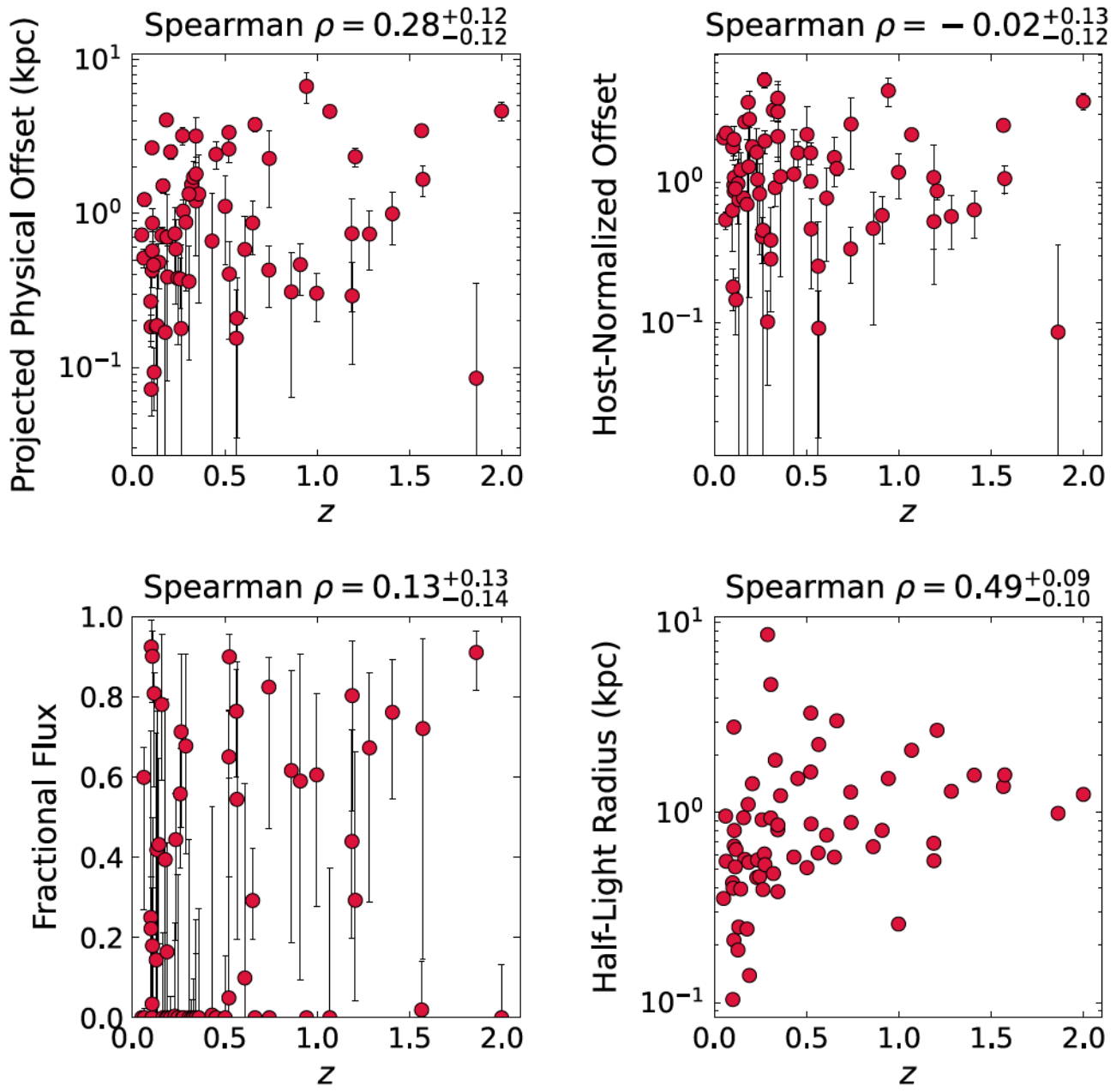

Figure 10. Physical offsets, host-normalized offsets, fractional flux values, and host half-light radii plotted as a function of redshift. In each panel we also list the Spearman's rank correlation coefficient. We find no clear correlations, with the most significant correlation being the one between half-light radius and redshift ($\rho \approx 0.49$).

somewhat older progenitors. However, this appears to be in conflict with the inferred preexplosion mass distribution of SLSNe, which points to systematically more-massive progenitors compared to SNe Ib/c (and the small number of LGRBs with inferred progenitor masses; Blanchard et al. 2020). Similarly, van den Heuvel & Portegies Zwart (2013) proposed a dynamical formation model in young dense star clusters for SLSNe and LGRBs, in which SLSNe are the product of multiple runaway collisions, but our results cast doubt on such a common formation path.

A possible explanation for the substantial fraction of SLSNe occurring outside of UV-bright regions is that their progenitors arise in disrupted binary systems, thereby gaining a velocity kick. As shown in Figures 6, 8, and 9 the dominant contribution to events at low fractional flux is from SLSNe at offsets of $R_{\rm norm} \sim 1$–4, or equivalently $R_{\rm phys} \sim 0.75$–3 kpc. Traveling such distances in the progenitor's lifetime of $\sim$10 Myr requires velocities of $\gtrsim 10^2\,{\rm km\,s^{-1}}$. Such high velocities may not be unexpected in models of runaway massive stars from disrupted binary systems, especially for a rare population in predominantly low-metallicity dwarf galaxies (e.g., Eldridge et al. 2011). While metallicity gradients in SLSN host galaxies could also reproduce the observed offset distribution, we note that such gradients are generally weak in nearby dwarf galaxies (e.g., Wang et al. 2019; Grossi et al. 2020). Therefore, the runaway star scenario is a more likely explanation.

The SLSN results are also reminiscent of the isolated locations of luminous blue variables (LBVs) in the Milky Way and Magellanic Clouds (Smith & Tombleson 2015), explained as possible evidence for LBV formation as mass gainers in

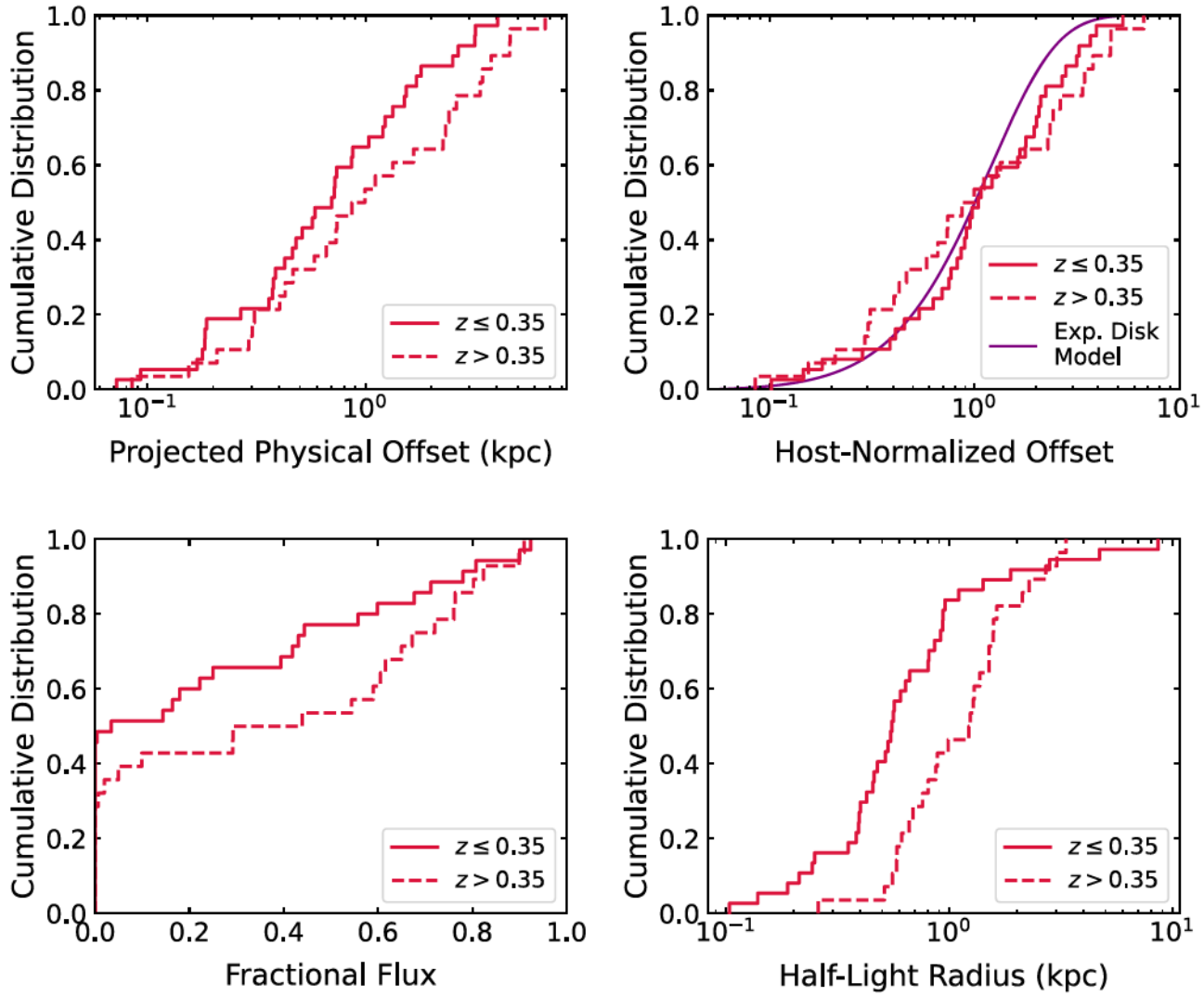

Figure 11. Cumulative distributions of physical offsets, host-normalized offsets, fractional flux values, and host half-light radii binned into two equal-size redshift ranges: $z \leqslant 0.35$ (solid) and $z > 0.35$ (dashed). We find a statistically significant trend in half-light radius, and a mild trend in fractional flux.

binary systems, which are subsequently disrupted. Such a scenario would explain both the large fraction of SLSNe outside of UV-bright regions, and the higher masses of their progenitors at the time of explosion compared to SNe Ib/c. Of course, stars exploding in the LBV phase, with an intact massive hydrogen envelope, cannot be the direct progenitors of SLSNe, but an analogous process involving disruption of a binary system after the progenitor's hydrogen envelope was stripped may be relevant.

Regardless of the exact formation pathway of SLSN progenitors, the offset and fractional flux distributions indicate that factors other than just progenitor mass and metallicity have a significant impact on their formation. However, the details of this pathway do not seem to influence the eventual SN explosion itself, as we do not find any obvious correlation between the SLSN locations and their explosion properties. This suggests that the explosion properties are mainly governed by the state of the progenitor preexplosion (e.g., mass or angular momentum).

6. Conclusions

We have carried out the most comprehensive study of the locations of SLSNe within their host galaxies to date using archival HST data for 65 SLSNe. We determine both the offset and fractional flux distributions for the sample, and compare these to other transients with massive-star progenitors (LGRBs and CCSNe). Our key findings are as follows.

1. SLSN host galaxies are more compact than the host galaxies of LGRBs (median of 0.76 versus 1.8 kpc, respectively) at large statistical significance (KS test p-value of 4.1×10^{-9}).
2. The host-normalized offsets of SLSNe have a median of 1.06 (in units of R_{50}; 90% confidence interval of 1.01–1.35 from a Monte Carlo simulation). The distribution overall traces an exponential disk profile, but with a significant overabundance of sources at $R_{\rm norm} \gtrsim 1.5$ not seen in the other transient populations. The host-normalized offsets are systematically larger than for LGRBs and CCSNe, with the closest match being SNe II.
3. The fractional flux distribution of SLSNe has a low median value of 0.16, with a 90% confidence interval of 37^{+6}_{-8}% of the sources being located in the dimmest UV regions. This distribution is strikingly different from those of LGRBs (with a preference for bright UV regions, with a median value of about 0.8) and CCSNe.

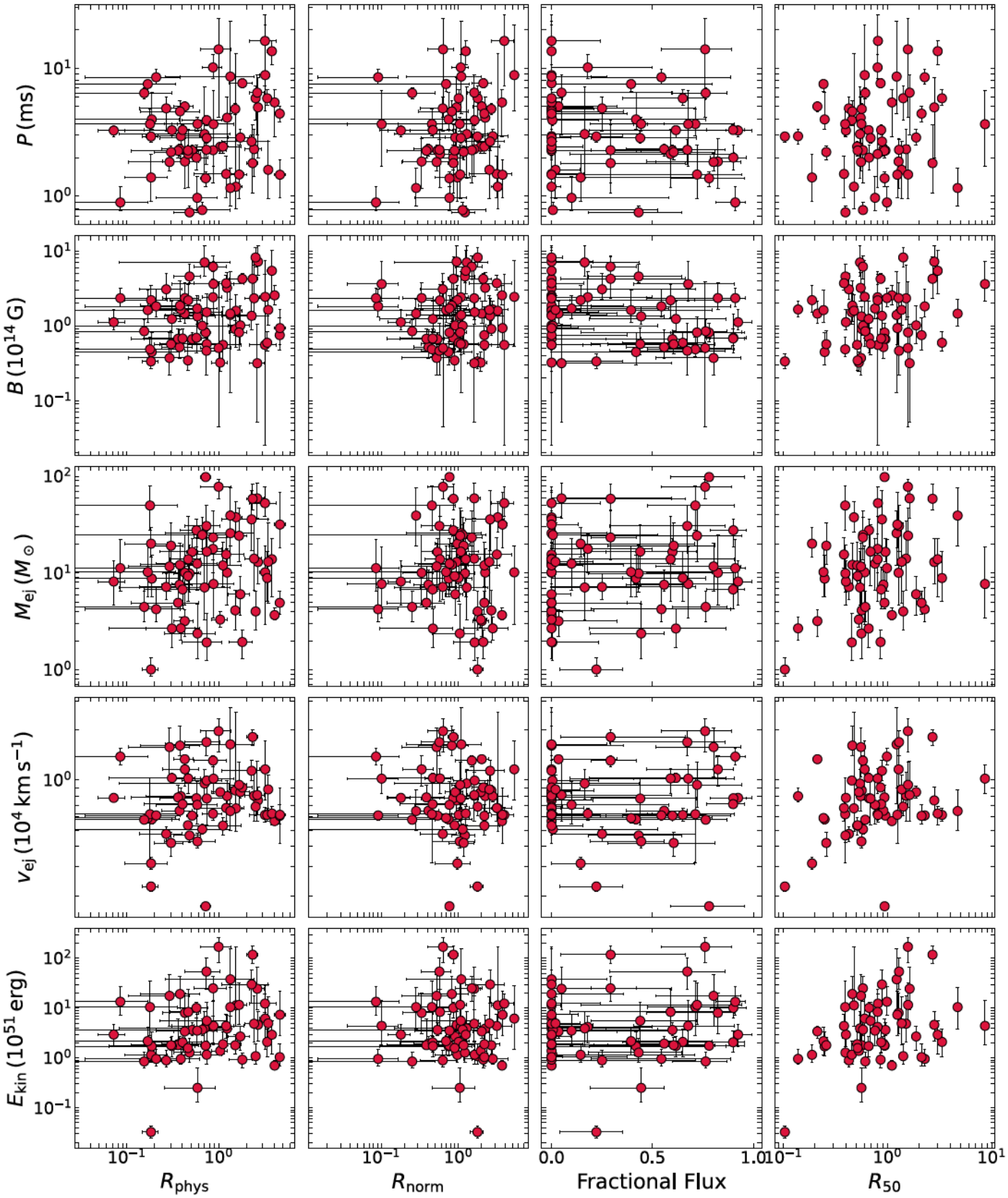

Figure 12. Magnetar model parameters (P, B, M_{ej}, v_{ej}, and E_{kin}), as well as observed peak luminosity (L_{peak}) and observed total radiated energy (E_{rad}), as a function of physical and host-normalized offsets, fractional flux values, and host half-light radii. The magnetar model parameters are from a uniform study using `MOSFiT` (Gomez et al. 2022). We do not find any significant correlation between the SLSN parameters and the SLSN environments.

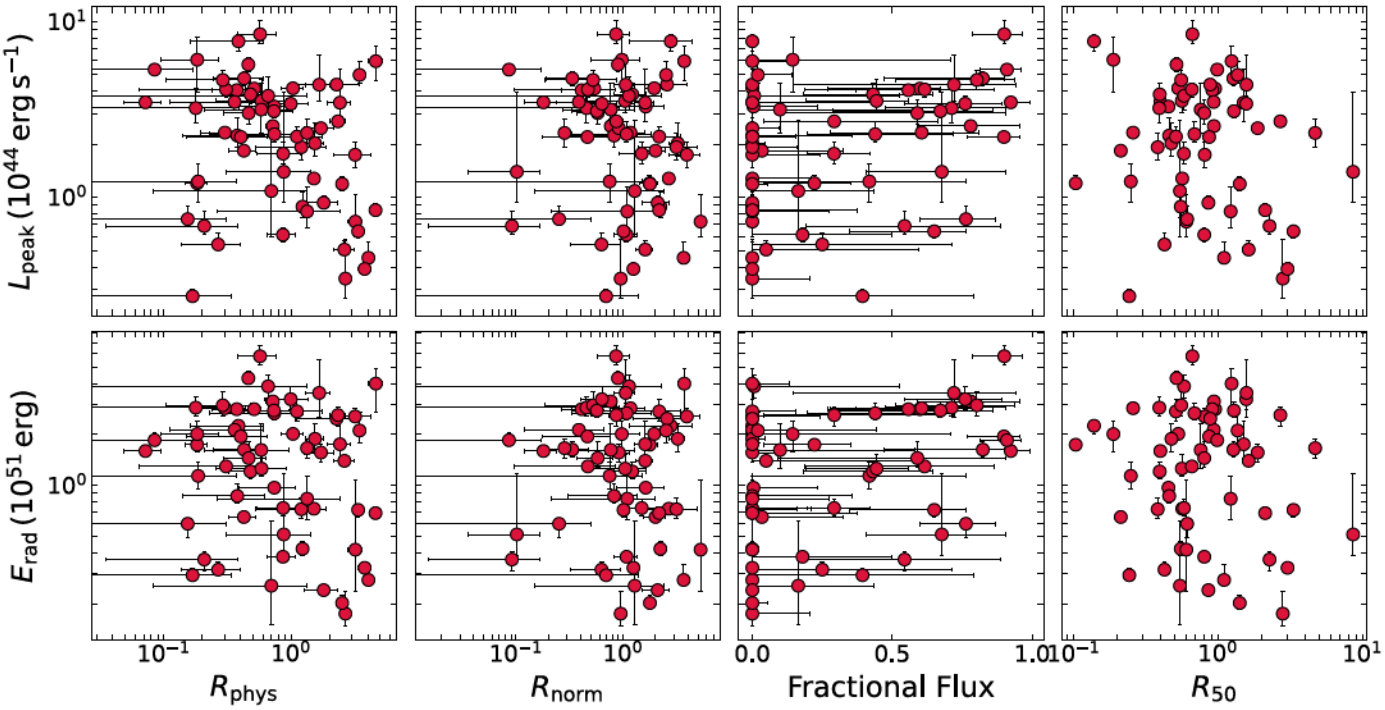

Figure 12. (Continued.)

4. The host-normalized offsets of SLSNe strongly correlate with their fractional fluxes, in a similar manner to those of LGRBs and CCSNe; the main distinction is the overabundance of SLSNe with fractional flux values of zero and normalized offsets of $R_{norm} \gtrsim 1$. We find that SLSNe with $R_{norm} \leqslant 1$ have a fractional flux distribution that linearly tracks the underlying UV light of their hosts, but about 60% of those with $R_{norm} > 1$ have fractional flux values of zero, in clear distinction from LGRBs and CCSNe with $R_{norm} > 1$.
5. The physical and normalized offsets, fractional flux values, and host half-light radii do not show statistically significant trends with redshift. When binned into low- ($z \leqslant 0.35$) and high-redshift ($z > 0.35$) ranges, however, the half-light radius distributions are statistically different, with lower-redshift SLSN hosts being systematically more compact.
6. There is no significant correlation between the locations of SLSNe and their explosion and magnetar engine parameters.
7. The substantial difference in SLSN and LGRB locations indicates that while both are rare classes of CCSNe most likely powered by central engines, their progenitors follow different formation pathways.
8. The large fraction of SLSNe outside of UV-bright regions may point to progenitors formed as runaway stars from disrupted binary systems with kick velocities of $\sim 10^2$ km s^{-1}.

With the upcoming Vera C. Rubin Observatory Legacy Survey of Space and Time, we expect a substantial increase in the SLSN discovery rate, extending to higher redshifts than at the present (e.g., Villar et al. 2018). Studies of this larger SLSN population with HST and JWST will be critical for exploring redshift trends, and perhaps subtle correlations between SLSN environments and their explosion properties that cannot be discerned in the current sample.

Acknowledgments

We thank Josh Grindlay, Daichi Hiramatsu, Ashley Villar, and Irwin Shapiro for helpful discussions and comments. We thank Mark Huber for providing images for PS1-MDS SLSNe, Charlotte Angus for providing images for a subset of DES SLSNe, and Matt Nicholl for supplying `galfit` models for SN 2015bn. The Berger Time Domain group at Harvard is supported in part by NSF and NASA grants, including support by the NSF under grant AST-2108531, as well as by the NSF under Cooperative Agreement PHY-2019786 (the NSF AI Institute for Artificial Intelligence and Fundamental Interactions http://iafi.org/). P.K.B. is supported by a CIERA Postdoctoral Fellowship. S.G. is supported by an STScI Postdoctoral Fellowship.

This research is based in part on observations made with the NASA/ESA Hubble Space Telescope obtained from the Space Telescope Science Institute, which is operated by the Association of Universities for Research in Astronomy, Inc., under NASA contract NAS 5-26555. These observations are associated with programs GO-9500, GO-12529, GO-12786, GO-13022, GO-13025, GO-13326, GO-13858, GO-14743, GO-15140, GO-15162, GO-15303, GO-15496, GO-16239, GO-16657, and GO-17181.

The Pan-STARRS1 Surveys have been made possible through contributions of the Institute for Astronomy, the University of Hawaii, the Pan-STARRS Project Office, the Max-Planck Society and its participating institutes, the Max Planck Institute for Astronomy, Heidelberg and the Max Planck Institute for Extraterrestrial Physics, Garching, The Johns Hopkins University, Durham University, the University of Edinburgh, Queen's University Belfast, the Harvard-Smithsonian Center for Astrophysics, the Las Cumbres Observatory Global Telescope

Network Incorporated, the National Central University of Taiwan, the Space Telescope Science Institute, the National Aeronautics and Space Administration under grant No. NNX08AR22G issued through the Planetary Science Division of the NASA Science Mission Directorate, the National Science Foundation under grant No. AST-1238877, the University of Maryland, and Eotvos Lorand University (ELTE).

This research has made use of the NASA/IPAC Infrared Science Archive, which is funded by the National Aeronautics and Space Administration and operated by the California Institute of Technology.

This research uses services or data provided by the Astro Data Lab at NSF's NOIRLab. NOIRLab is operated by the Association of Universities for Research in Astronomy (AURA), Inc. under a cooperative agreement with the National Science Foundation.

This project used public archival data from the Dark Energy Survey (DES) as distributed by the Astro Data Archive at NSF's NOIRLab. Funding for the DES Projects has been provided by the US Department of Energy, the US National Science Foundation, the Ministry of Science and Education of Spain, the Science and Technology Facilities Council of the United Kingdom, the Higher Education Funding Council for England, the National Center for Supercomputing Applications at the University of Illinois at Urbana-Champaign, the Kavli Institute for Cosmological Physics at the University of Chicago, Center for Cosmology and Astro-Particle Physics at the Ohio State University, the Mitchell Institute for Fundamental Physics and Astronomy at Texas A&M University, Financiadora de Estudos e Projetos, Fundação Carlos Chagas Filho de Amparo à Pesquisa do Estado do Rio de Janeiro, Conselho Nacional de Desenvolvimento Científico e Tecnológico and the Ministério da Ciência, Tecnologia e Inovação, the Deutsche Forschungsgemeinschaft and the Collaborating Institutions in the Dark Energy Survey. The Collaborating Institutions are Argonne National Laboratory, the University of California at Santa Cruz, the University of Cambridge, Centro de Investigaciones Enérgeticas, 22 Medioambientales y Tecnológicas- Madrid, the University of Chicago, University College London, the DES-Brazil Consortium, the University of Edinburgh, the Eidgenössische Technische Hochschule (ETH) Zürich, Fermi National Accelerator Laboratory, the University of Illinois at Urbana-Champaign, the Institut de Ciències de l'Espai (IEEC/CSIC), the Institut de Física d'Altes Energies, Lawrence Berkeley National Laboratory, the Ludwig-Maximilians Universität München and the associated Excellence Cluster Universe, the University of Michigan, the NSF's NOIRLab, the University of Nottingham, the Ohio State University, the OzDES Membership Consortium, the University of Pennsylvania, the University of Portsmouth, SLAC National Accelerator Laboratory, Stanford University, the University of Sussex, and Texas A&M University.

The Liverpool Telescope is operated on the island of La Palma by Liverpool John Moores University in the Spanish Observatorio del Roque de los Muchachos of the Instituto de Astrofisica de Canarias with financial support from the UK Science and Technology Facilities Council.

Based in part on observations obtained at the international Gemini Observatory, a program of NSF's NOIRLab, which is managed by the Association of Universities for Research in Astronomy (AURA) under a cooperative agreement with the National Science Foundation on behalf of the Gemini Observatory partnership: the National Science Foundation (United States), National Research Council (Canada), Agencia Nacional de Investigación y Desarrollo (Chile), Ministerio de Ciencia, Tecnología e Innovación (Argentina), Ministério da Ciência, Tecnologia, Inovações e Comunicações (Brazil), and Korea Astronomy and Space Science Institute (Republic of Korea).

This paper includes data gathered with the 6.5 m Magellan Telescopes located at Las Campanas Observatory, Chile. Observations reported here were obtained at the MMT Observatory, a joint facility of the University of Arizona and the Smithsonian Institution. This work has made use of data from the European Space Agency (ESA) mission Gaia (https://www.cosmos.esa.int/gaia), processed by the Gaia Data Processing and Analysis Consortium (DPAC; https://www.cosmos.esa.int/web/gaia/dpac/consortium). Funding for the DPAC has been provided by national institutions, in particular the institutions participating in the Gaia Multilateral Agreement.

Facilities: Blanco (DECam), Gemini: South (GMOS), HST (ACS, WFC3), iPTF, Magellan: Baade (IMACS), MMT (Binospec), PS1, PTF, and ZTF.

Software: AstroDrizzle (Gonzaga et al. 2012), Astropy (Astropy Collaboration et al. 2013, 2018), Matplotlib (Hunter 2007), NumPy (Harris et al. 2020), Photutils (Bradley et al. 2022), pymccorrelation (Curran 2014; Privon et al. 2020), PyZOGY (Zackay et al. 2016), and Scipy (Virtanen et al. 2020).

Appendix A
Host Galaxy Nondetections

In Figure 13 we show the HST images for the 19 SLSNe without a detected host galaxy.

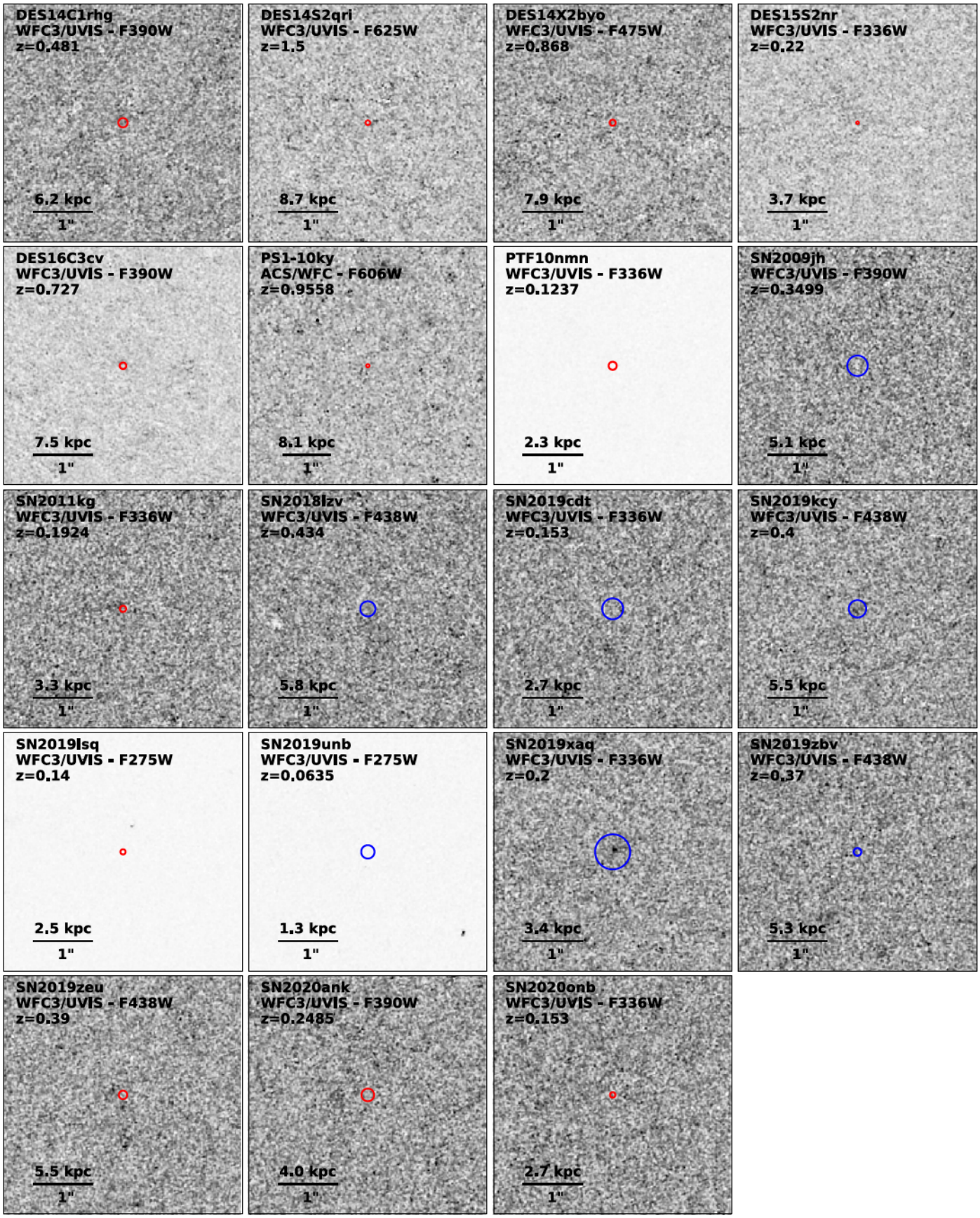

Figure 13. HST drizzled images of 19 SLSNe with available SN imaging and successful astrometric alignment, but no detected host. The images are centered on the centroid location of the SLSNe and aligned with north up and east to the left. Solid circles indicating the locations of the SLSNe, with a radius corresponding to 1σ uncertainty. Red and blue circles indicate the positions determined using relative and absolute astrometry, respectively.

Appendix B
Offset Corrections

Since offsets are a positive-definite quantity, sources with a large offset uncertainty may also be systematically skewed to larger offset values. Since the offset uncertainty σ_R ($\sigma_{R_{\rm phys}}$ or $\sigma_{R_{\rm norm}}$) is not a physical property related to the offset R ($R_{\rm phys}$ or $R_{\rm norm}$) itself, but rather is solely due to measurement uncertainties, there should be no correlation between R and σ_R. In Figure 14 we plot $\sigma_{R_{\rm phys}}$ versus $R_{\rm phys}$ and $\sigma_{R_{\rm norm}}$ versus $R_{\rm norm}$, and find a mild correlation, which is specifically due to the apparent lack of sources with large uncertainties and small offsets; this is exactly the systematic effect described above.

To quantify the impact of this effect we experiment with a simple procedure to determine a correction factor for each host-normalized offset value, using the exponential disk distribution. First, we draw 100,000 random offset values from the exponential disk profile and assign to each an uncertainty drawn from a log-uniform distribution spanning $\sigma_{R_{\rm norm}} = 10^{-3}$–10. This provides an input "intrinsic" population; see the left panel of Figure 15. Second, we reconstruct a Rice distribution for each offset-uncertainty data point using Equation (2), and randomly draw a point from the distribution. This "shifted" population (middle panel of Figure 15) is empirically equivalent to what we measure and report in Section 4.1 and Section 4.3. Lastly, we track the peak of the distribution at each uncertainty value for both the intrinsic and shifted populations, and use the resulting ratio to determine a mean correction factor as a function of $\sigma_{R_{\rm norm}}$; see the right panel of Figure 15. This correction factor is $\gtrsim$1 only at $\sigma_{R_{\rm norm}} \gtrsim 1$. Finally, we apply this correction factor to the observed SLSN offset distributions, as shown by the dashed lines in Figures 3 and 5. Overall, we find that this correction is rather minimal and does not affect the results of our study; the corrected $R_{\rm norm}$ distribution has a slightly lower median of 0.93 versus 1.06 for the measured distribution. We also note that none of the other comparison samples (LGRBs and SNe) have been subjected to this analysis so it is likely that a correction would shift all populations by a comparable amount.

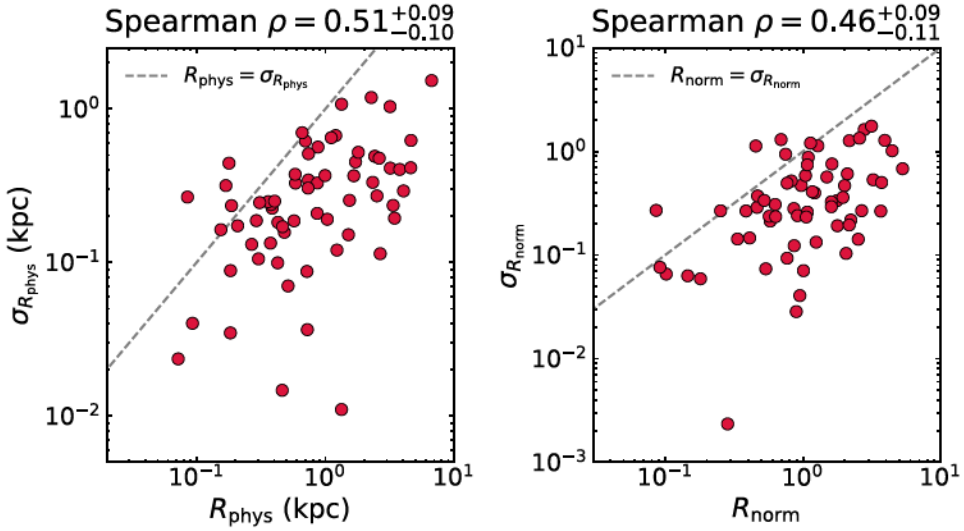

Figure 14. Left: physical offset uncertainty ($\sigma_{R_{\rm phys}}$) vs. physical offset ($R_{\rm phys}$). Right: host-normalized offset uncertainty ($\sigma_{R_{\rm norm}}$) vs. host-normalized offset ($R_{\rm norm}$). The dashed line in each panel indicates the 1:1 line where the offset is equal to its uncertainty. The dearth of sources with small offsets and large uncertainties (the upper left quadrant of each panel) is due to the positive-definite nature of the offset quantity.

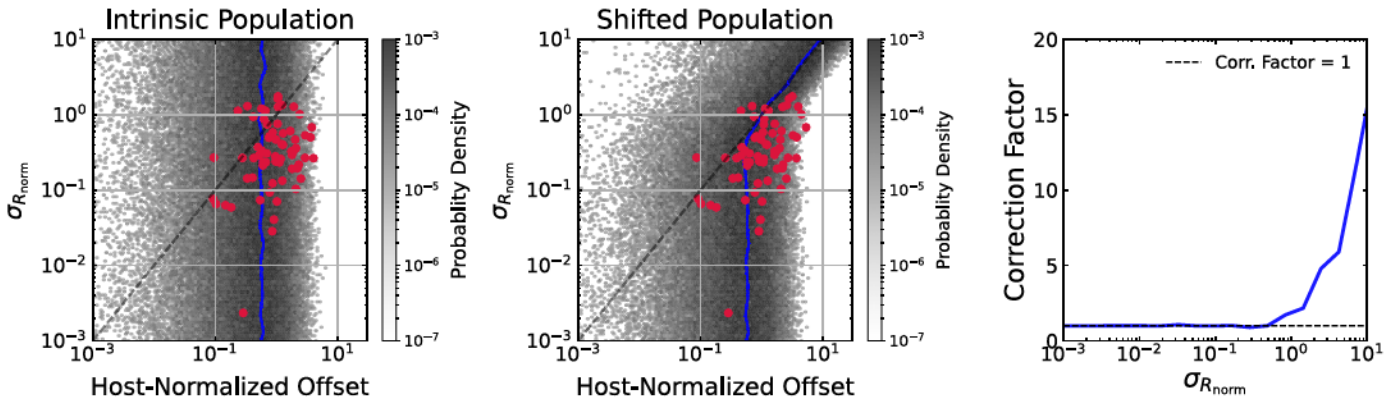

Figure 15. Left: 2D probability density plot showing the host-normalized offsets for a population drawn from an exponential disk profile with randomly assigned uncertainties. The blue line marks the peak value as a function of $\sigma_{R_{\rm norm}}$. Plotted in red are the "corrected" $R_{\rm norm}$ values for SLSNe. Middle: 2D probability density plot showing the host-normalized offsets after sampling with the Rice distribution. The blue line marks the peak value as a function of $\sigma_{R_{\rm norm}}$; the distribution is clearly skewed to larger values of $R_{\rm norm}$ at larger $\sigma_{R_{\rm norm}}$. Plotted in red are the measured values for SLSNe. Right: the mean correction factor as a function of $\sigma_{R_{\rm norm}}$ is calculated as the ratio of the peaks (blue lines) between the two populations.

ORCID iDs

Brian Hsu https://orcid.org/0000-0002-9454-1742
Peter K. Blanchard https://orcid.org/0000-0003-0526-2248
Edo Berger https://orcid.org/0000-0002-9392-9681
Sebastian Gomez https://orcid.org/0000-0001-6395-6702

References

Anderson, J. P., Habergham, S. M., James, P. A., & Hamuy, M. 2012, MNRAS, 424, 1372
Anderson, J. P., James, P. A., Habergham, S. M., Galbany, L., & Kuncarayakti, H. 2015, PASA, 32, e019
Anderson, T. W., & Darling, D. A. 1952, Ann. Math. Stat., 23, 193
Angus, C. R., Levan, A. J., Perley, D. A., et al. 2016, MNRAS, 458, 84
Angus, C. R., Smith, M., Sullivan, M., et al. 2019, MNRAS, 487, 2215
Arnett, W. D. 1982, ApJ, 253, 785
Astropy Collaboration, Price-Whelan, A. M., Sipőcz, B. M., et al. 2018, AJ, 156, 123
Astropy Collaboration, Robitaille, T. P., Tollerud, E. J., et al. 2013, A&A, 558, A33
Barbarino, C., Sollerman, J., Taddia, F., et al. 2020, arXiv:2010.08392
Bellm, E. C., Kulkarni, S. R., Barlow, T., et al. 2019, PASP, 131, 068003
Berger, E. 2010, ApJ, 722, 1946
Blanchard, P. K., Berger, E., & Fong, W. 2016, ApJ, 817, 144
Blanchard, P. K., Berger, E., Nicholl, M., et al. 2021, ApJ, 921, 64
Blanchard, P. K., Berger, E., Nicholl, M., & Villar, V. A. 2020, ApJ, 897, 114
Bloom, J. S., Kulkarni, S. R., & Djorgovski, S. G. 2002, AJ, 123, 1111
Bradley, L., Sipőcz, B., Robitaille, T., et al. 2022, astropy/photutils: 1.5.0, v1.5.0, Zenodo, doi:10.5281/zenodo.6825092
Chambers, K. C., Magnier, E. A., Metcalfe, N., et al. 2016, arXiv:1612.05560
Chatzopoulos, E., Wheeler, J. C., & Vinko, J. 2012, ApJ, 746, 121
Chen, T.-W., Smartt, S. J., Bresolin, F., et al. 2013, ApJL, 763, L28
Chen, Z. H., Yan, L., Kangas, T., et al. 2022a, ApJ, 943, 41
Chen, Z. H., Yan, L., Kangas, T., et al. 2022b, ApJ, 943, 42
Chevalier, R. A., & Irwin, C. M. 2011, ApJL, 729, L6
Chomiuk, L., Chornock, R., Soderberg, A. M., et al. 2011, ApJ, 743, 114
Cikota, A., De Cia, A., Schulze, S., et al. 2017, MNRAS, 469, 4705
Curran, P. A. 2014, arXiv:1411.3816
Dark Energy Survey Collaboration 2005, arXiv:astro-ph/0510346
Dark Energy Survey Collaboration 2016, MNRAS, 460, 1270
De Cia, A., Gal-Yam, A., Rubin, A., et al. 2018, ApJ, 860, 100
Dessart, L., Hillier, D. J., Waldman, R., Livne, E., & Blondin, S. 2012, MNRAS, 426, L76
Eftekhari, T., Margalit, B., Omand, C. M. B., et al. 2021, ApJ, 912, 21
Eldridge, J. J., Langer, N., & Tout, C. A. 2011, MNRAS, 414, 3501
Fong, W., & Berger, E. 2013, ApJ, 776, 18
Frohmaier, C., Angus, C. R., Vincenzi, M., et al. 2021, MNRAS, 500, 5142
Fruchter, A. S., Levan, A. J., Strolger, L., et al. 2006, Natur, 441, 463
Gaia Collaboration, Prusti, T., & de Bruijne, J. H. J. 2016, A&A, 595, A1
Gaia Collaboration, Vallenari, A., Brown, A. G. A., et al. 2023, A&A, 674, A1
Gal-Yam, A. 2012, Sci, 337, 927
Gal-Yam, A. 2019, ApJ, 882, 102
Gomez, S., Berger, E., Blanchard, P. K., et al. 2020, ApJ, 904, 74
Gomez, S., Berger, E., Hosseinzadeh, G., et al. 2021, ApJ, 913, 143
Gomez, S., Berger, E., Nicholl, M., Blanchard, P. K., & Hosseinzadeh, G. 2022, ApJ, 941, 107
Gonzaga, S., Hack, W., Fruchter, A., & Mack, J. 2012, The DrizzlePac Handbook (Baltimore, MD: STScI)
Gordon, K. D., Clayton, G. C., Decleir, M., et al. 2023, ApJ, 950, 86
Grossi, M., García-Benito, R., Cortesi, A., et al. 2020, MNRAS, 498, 1939
Guillochon, J., Nicholl, M., Villar, V. A., et al. 2018, ApJS, 236, 6
Harris, C.R., Millman, K. J., van der Walt, S. J., et al. 2020, Natur, 585, 357
Hsu, B., Hosseinzadeh, G., & Berger, E. 2021, ApJ, 921, 180
Hunter, J. D. 2007, CSE, 9, 90
Inserra, C., Nicholl, M., Chen, T. W., et al. 2017, MNRAS, 468, 4642
Inserra, C., Smartt, S. J., Jerkstrand, A., et al. 2013, ApJ, 770, 128
IRSA 2022, Zwicky Transient Facility Image Service IPAC, doi:10.26131/IRSA539
Jerkstrand, A., Smartt, S. J., Inserra, C., et al. 2017, ApJ, 835, 13
Kasen, D., & Bildsten, L. 2010, ApJ, 717, 245
Kelly, P. L., & Kirshner, R. P. 2012, ApJ, 759, 107
Kelly, P. L., Kirshner, R. P., & Pahre, M. 2008, ApJ, 687, 1201
Liu, Y.-Q., Modjaz, M., & Bianco, F. B. 2017, ApJ, 845, 85
Liu, Z.-W., Tauris, T. M., Röpke, F. K., et al. 2015, A&A, 584, A11
Lunnan, R., Chornock, R., Berger, E., et al. 2013, ApJ, 771, 97
Lunnan, R., Chornock, R., Berger, E., et al. 2014, ApJ, 787, 138
Lunnan, R., Chornock, R., Berger, E., et al. 2015, ApJ, 804, 90
Lunnan, R., Chornock, R., Berger, E., et al. 2018, ApJ, 852, 81
Margutti, R., Chornock, R., Metzger, B. D., et al. 2018, ApJ, 864, 45
Mazzali, P. A., Sullivan, M., Pian, E., Greiner, J., & Kann, D. A. 2016, MNRAS, 458, 3455
Metzger, B. D., Margalit, B., Kasen, D., & Quataert, E. 2015, MNRAS, 454, 3311
Moriya, T. J., Liu, Z.-W., Mackey, J., Chen, T.-W., & Langer, N. 2015, A&A, 584, L5
Nicholl, M., Berger, E., Blanchard, P. K., Gomez, S., & Chornock, R. 2019, ApJ, 871, 102
Nicholl, M., Berger, E., Margutti, R., et al. 2016, ApJL, 828, L18
Nicholl, M., Berger, E., Margutti, R., et al. 2017a, ApJL, 845, L8
Nicholl, M., Berger, E., Margutti, R., et al. 2017b, ApJL, 835, L8
Nicholl, M., Blanchard, P. K., Berger, E., et al. 2018, ApJL, 866, L24
Nicholl, M., Guillochon, J., & Berger, E. 2017c, ApJ, 850, 55
Nicholl, M., Smartt, S. J., Jerkstrand, A., et al. 2013, Natur, 502, 346
Nicholl, M., Smartt, S. J., Jerkstrand, A., et al. 2015, MNRAS, 452, 3869
Oke, J. B., & Gunn, J. E. 1983, ApJ, 266, 713
Pastorello, A., Smartt, S. J., Botticella, M. T., et al. 2010, ApJL, 724, L16
Peng, C. Y., Ho, L. C., Impey, C. D., & Rix, H.-W. 2010, AJ, 139, 2097
Perley, D. A., Fremling, C., Sollerman, J., et al. 2020, ApJ, 904, 35
Perley, D. A., Quimby, R. M., Yan, L., et al. 2016, ApJ, 830, 13
Planck Collaboration, Aghanim, N., Akrami, Y., et al. 2020, A&A, 641, A6
Prieto, J. L., Stanek, K. Z., & Beacom, J. F. 2008, ApJ, 673, 999
Privon, G. C., Ricci, C., Aalto, S., et al. 2020, ApJ, 893, 149
PTF Team 2020, Palomar Transient Factory Level 1, IPAC, doi:10.26131/IRSA155
Quimby, R. M., De Cia, A., Gal-Yam, A., et al. 2018, ApJ, 855, 2
Quimby, R. M., Kulkarni, S. R., Kasliwal, M. M., et al. 2011, Natur, 474, 487
Rau, A., Kulkarni, S. R., Law, N. M., et al. 2009, PASP, 121, 1334
Schlafly, E. F., & Finkbeiner, D. P. 2011, ApJ, 737, 103
Schulze, S., Krühler, T., Leloudas, G., et al. 2018, MNRAS, 473, 1258
Smirnov, N. 1948, Ann. Math. Stat., 19, 279
Smith, N., & Tombleson, R. 2015, MNRAS, 447, 598
Spearman, C. 1904, Am. J. Psychol., 15, 72
Steele, I. A., Smith, R. J., Rees, P. C., et al. 2004, Proc. SPIE, 5489, 679
Stevance, H. F., & Eldridge, J. J. 2021, MNRAS, 504, L51
Svensson, K. M., Levan, A. J., Tanvir, N. R., Fruchter, A. S., & Strolger, L. G. 2010, MNRAS, 405, 57
Taggart, K., & Perley, D. A. 2021, MNRAS, 503, 3931
van den Heuvel, E. P. J., & Portegies Zwart, S. F. 2013, ApJ, 779, 114
Villar, V. A., Berger, E., Miller, G., et al. 2019, ApJ, 884, 83
Villar, V. A., Nicholl, M., & Berger, E. 2018, ApJ, 869, 166
Virtanen, P., Gommers, R., Oliphant, T. E., et al. 2020, NatMe, 17, 261
Wang, X., Jones, T. A., Treu, T., et al. 2019, ApJ, 882, 94
Wang, X., Wang, L., Filippenko, A. V., Zhang, T., & Zhao, X. 2013, Sci, 340, 170
Woosley, S. E. 2010, ApJL, 719, L204
Yan, L., Lunnan, R., Perley, D. A., et al. 2017a, ApJ, 848, 6
Yan, L., Quimby, R., Gal-Yam, A., et al. 2017b, ApJ, 840, 57
Yan, L., Quimby, R., Ofek, E., et al. 2015, ApJ, 814, 108
Zackay, B., Ofek, E. O., & Gal-Yam, A. 2016, ApJ, 830, 27